

NAVAL POSTGRADUATE SCHOOL Monterey , California



THESIS

ACOUSTIC TOMOGRAPHY IN THE GREENLAND
SEA

by

John E. Joseph

June 1991

Thesis Advisor
Co-Advisor

Ching-Sang Chiu
Jeffrey A. Nystuen

Approved for public release; distribution is unlimited.

T256213

REPORT DOCUMENTATION PAGE				
1a Report Security Classification Unclassified			1b Restrictive Markings	
2a Security Classification Authority			3 Distribution Availability of Report Approved for public release; distribution is unlimited.	
2b Declassification Downgrading Schedule				
4 Performing Organization Report Number(s)			5 Monitoring Organization Report Number(s)	
6a Name of Performing Organization Naval Postgraduate School		6b Office Symbol (if applicable) 35	7a Name of Monitoring Organization Naval Postgraduate School	
6c Address (city, state, and ZIP code) Monterey, CA 93943-5000			7b Address (city, state, and ZIP code) Monterey, CA 93943-5000	
8a Name of Funding Sponsoring Organization		8b Office Symbol (if applicable)	9 Procurement Instrument Identification Number	
8c Address (city, state, and ZIP code)			10 Source of Funding Numbers	
			Program Element No	Project No
11 Title (include security classification) ACOUSTIC TOMOGRAPHY IN THE GREENLAND SEA				
12 Personal Author(s) John E. Joseph				
13a Type of Report Master's Thesis		13b Time Covered From To		15 Page Count 64
		14 Date of Report (year, month, day) June 1991		
16 Supplementary Notation The views expressed in this thesis are those of the author and do not reflect the official policy or position of the Department of Defense or the U.S. Government.				
17 Cosati Codes			18 Subject Terms (continue on reverse if necessary and identify by block number) Acoustic tomography, Ocean acoustics	
Field	Group	Subgroup		
19 Abstract (continue on reverse if necessary and identify by block number) <p>As part of the international Greenland Sea Project, Woods Hole Oceanographic Institute and Scripps Institution of Oceanography deployed a six transeiver ocean acoustic tomography array to monitor ocean ventilation and circulation over the 1988-89 winter cooling season. A stochastic inverse method computer code which attains a solution by minimizing mean square error is used to perform inversions of the Greenland Sea tomography data.</p> <p>A computer simulated ocean is used to evaluate various aspects of system performance. We first consider the advantages and problems associated with using a ray theory based algorithm to establish the forward problem for the Greenland Sea tomography array. Next, we made two adjustments to our inversion code and discuss the effects on system performance. The first adjustment allows for layers of different thicknesses in the inverse solution to increase the density of estimates in regions of interest. The second adjustment allows the estimator to expect variability of the unknown field to decrease exponentially with depth.</p> <p>Our results show the ray theory based algorithm is an adequate method of modeling ray paths in the Greenland Sea, but has limitations. Reliability of ray paths degrades as launch angles become shallower and if strong gradients and rapidly changing gradients in sound speed are present in the vicinity of the transeiver elements. We also find varying the thickness of layers in the solution allows us to examine the more variable upper ocean in greater detail without increasing computational effort. However, this adjustment alone has the undesirable side effect of shifting system resolution towards the lower ocean. This shift in resolution is offset by informing the estimator about the vertical variability distribution of the unknown field. This <i>a priori</i> knowledge is parameterized by the covariance function of the unknown field. Uncertainty in knowing the true variability distribution affects model performance. The inverse solution is more sensitive to underestimating than overestimating the true value of folding depth. The model is also more sensitive to both underestimation and overestimation at small true folding depths.</p> <p>A set of Greenland Sea data between one transeiver pair was processed by Woods Hole Oceanographic Institute. Although only three groups of eigenrays are involved, initial inversion results indicate the estimator detects seasonal changes and synoptic scale events occurring at time scales greater than 20 days, however, solutions show wide fluctuations at time scales shorter than 20 days.</p>				
20 Distribution Availability of Abstract <input checked="" type="checkbox"/> unclassified unlimited <input type="checkbox"/> same as report <input type="checkbox"/> DTIC users			21 Abstract Security Classification Unclassified	
22a Name of Responsible Individual Ching-Sang Chiu			22b Telephone (include Area code) (408) 646-3239	22c Office Symbol OC/Ci

Approved for public release; distribution is unlimited.

Acoustic Tomography in the Greenland Sea

by

John E. Joseph

Lieutenant, United States Navy

M.S., Radford University, 1979

B.A., Virginia Polytechnic Institute and State University, 1976

Submitted in partial fulfillment of the
requirements for the degree of

MASTER OF SCIENCE IN PHYSICAL OCEANOGRAPHY AND
METEOROLOGY

from the

NAVAL POSTGRADUATE SCHOOL

June 1991

ABSTRACT

As part of the international Greenland Sea Project, Woods Hole Oceanographic Institute and Scripps Institution of Oceanography deployed a six transceiver ocean acoustic tomography array to monitor ocean ventilation and circulation over the 1988-89 winter cooling season. A stochastic inverse method computer code which attains a solution by minimizing mean square error is used to perform inversions of the Greenland Sea tomography data.

A computer simulated ocean is used to evaluate various aspects of system performance. We first consider the advantages and problems associated with using a ray theory based algorithm to establish the forward problem for the Greenland Sea tomography array. Next, we made two adjustments to our inversion code and discuss the effects on system performance. The first adjustment allows for layers of different thicknesses in the inverse solution to increase the density of estimates in regions of interest. The second adjustment allows the estimator to expect variability of the unknown field to decrease exponentially with depth.

Our results show the ray theory based algorithm is an adequate method of modeling ray paths in the Greenland Sea, but has limitations. Reliability of ray paths degrades as launch angles become shallower and if strong gradients and rapidly changing gradients in sound speed are present in the vicinity of the transceiver elements. We also find varying the thickness of layers in the solution allows us to examine the more variable upper ocean in greater detail without increasing computational effort. However, this adjustment alone has the undesirable side effect of shifting system resolution towards the lower ocean. This shift in resolution is offset by informing the estimator about the vertical variability distribution of the unknown field. This *a priori* knowledge is parameterized by the covariance function of the unknown field. Uncertainty in knowing the true variability distribution affects model performance. The inverse solution is more sensitive to underestimating than overestimating the true value of folding depth. The model is also more sensitive to both underestimation and overestimation at small true folding depths.

A set of Greenland Sea data between one transceiver pair was processed by Woods Hole Oceanographic Institute. Although only three groups of eigenrays are involved, initial inversion results indicate the estimator detects seasonal changes and synoptic scale

178513
J8264/
C1

events occurring at time scales greater than 20 days, however, solutions show wide fluctuations at time scales shorter than 20 days.

ACKNOWLEDGEMENTS

Participating in research in ocean acoustic tomography has rewarded me with a great deal of intellectual growth and stimulation. There are several people to whom I owe many thanks for the success I have had in completing this thesis.

I would like to thank my advisors, Dr. Ching-Sang Chiu and Dr. Jeff Nystuen, who opened my eyes to the interesting world of tomography. Their expert guidance and patience from the beginning have allowed my understanding of this exciting field to increase by orders of magnitude. I wish to thank Dr. Jim Lynch and Mr. Rich Pawlowicz of Woods Hole Oceanographic Institute for providing the processed Greenland Sea data used in this work. I thank Dr. Jim Miller for his suggestions and assistance on various aspects of this work.

I sincerely thank Arlene Guest, Bob Edson and Pedro Tsai. I owe much to them for their unselfish assistance in my computer related work. They made life a lot easier.

The love of my family has always been a source of endless support and I wish to thank them. The support of friends has proven invaluable as well. Many fruitful discussions arose during SeaSlug postgame debriefs.

Finally, I wish to thank my dearest friend, Kathleen Pierce, whose unselfish support and love has been truly inspirational.

TABLE OF CONTENTS

I. INTRODUCTION	1
A. OCEAN ACOUSTIC TOMOGRAPHY	1
B. THE GREENLAND SEA PROJECT	2
C. THESIS OBJECTIVES	2
II. OVERVIEW OF ACOUSTIC TOMOGRAPHY PRINCIPLES	6
A. THE FORWARD PROBLEM	6
B. THE INVERSE PROBLEM	10
1. The Estimator	10
2. Measurement of Error	11
3. Measurement of Resolution	12
III. EIGENRAY PREDICTION AND INVERSION CODE DEVELOPMENT	15
A. EIGENRAY PATH PREDICTION	15
B. VERTICAL LAYERS AND RMS VARIABILITY DISTRIBUTION	22
IV. PRELIMINARY INVERSIONS USING GREENLAND SEA DATA	34
V. CONCLUSIONS AND RECOMMENDATIONS	49
A. CONCLUSIONS	49
B. RECOMMENDATIONS	50
REFERENCES	52
INITIAL DISTRIBUTION LIST	54

LIST OF TABLES

Table 1.	TRANSCIVER LOCATIONS	2
Table 2.	MOORING RANGES (KM) AND RANGE ERRORS (M)	4
Table 3.	SYSTEM PARAMETERS	36

LIST OF FIGURES

Figure 1.	Planned Deployment Site of the Greenland Sea Tomography Array	3
Figure 2.	Path Segment Geometry Through Significant Points	17
Figure 3.	CTD Data at Mooring 6 on Yearday 264	18
Figure 4.	Near Surface Sound Speed Profiles	20
Figure 5.	Sound Speed Effects on Eigenray Paths	21
Figure 6.	Plan View of Array Geometry	23
Figure 7.	Eigenray Paths along Vertical Slices	24
Figure 8.	Resolution Kernel Peak Values (VTL approach)	25
Figure 9.	Resolution Kernel Peak Values (EQS approach)	26
Figure 10.	Resolution Kernel Peak Values Using Depth Dependent Variability	27
Figure 11.	Standard Deviation of the Estimate (m s)	28
Figure 12.	Depth Dependent Variability Curves at Various Folding Depths	29
Figure 13.	Perturbation Estimator Response Using Various Folding Depths	31
Figure 14.	Half-depth as a Function of Folding Depth	32
Figure 15.	Current Estimator Response Using Various Folding Depths	33
Figure 16.	Vertical Slice and Eigenray Paths for Moorings 4 and 5	35
Figure 17.	Resolution Kernel Peak Values for Greenland Sea Data Inversion	37
Figure 18.	Y-Direction Minimum Resolution Length (km)	38
Figure 19.	Z-Direction Minimum Resolution Length (m)	39
Figure 20.	Percent RMS Error	40
Figure 21.	Sound Speed Perturbations of the Time Averaged Ocean (m/s)	42
Figure 22.	Sound Speed Estimates and Temperature Data Near Mooring 4	43
Figure 23.	Sound Speed Estimates and Temperature Data Near Mooring 5	44
Figure 24.	Sound Speed Perturbation Estimates (m/s), Yearday 462	45
Figure 25.	Sound Speed Perturbation Estimates (m/s), Yearday 465	46
Figure 26.	Sound Speed Perturbation Estimates (m/s), Yearday 468	46
Figure 27.	Sound Speed Perturbation Estimates (m/s), Yearday 471	47
Figure 28.	Sound Speed Perturbation Estimates (m/s), Yearday 474	47
Figure 29.	Sound Speed Perturbation Estimates (m/s), Yearday 477	48
Figure 30.	Sound Speed Perturbation Estimates (m/s), Yearday 480	48

I. INTRODUCTION

A. OCEAN ACOUSTIC TOMOGRAPHY

Tomography is a method to remotely sense interior structures. It uses electromagnetic, seismic, or sound waves to propagate through and probe relatively transparent media. For example, x-rays are commonly used in medical computer assisted tomography (CAT) scans and seismic waves induced by surface sources are used to study the interior of the earth (Backus and Gilbert, 1967). Using analogous methods, Munk and Wunsch (1979) introduced ocean acoustic tomography as a means of monitoring mesoscale fluctuations in ocean basins. Sound waves, which are sensitive to density changes and currents but transit well through the ocean, gather information as they encounter structures in the ocean interior. The data is received in the form of a perturbed travel time from a source to a receiver. Using inverse techniques, the best estimate as to what structure could result in the observed data is constructed.

Ocean acoustic tomography has several practical advantages over conventional hydrographic study techniques, as cited by Chiu *et al.* (1987). The monitoring system can be established as a semipermanent, continuous observing system which is not greatly affected by weather. It has high temporal resolution and can cover an extensive volume of ocean simultaneously with only a few moorings, which reduces deployment and maintenance costs. Another advantage stated by Munk and Wunsch (1979) is that the amount of additional information gained by each additional mooring increases more rapidly than that gained by additional "spot" measurements since each mooring sets up distinct new paths to each of the previously set moorings. The gain in spot measurements is more or less linear with the number of instruments deployed.

Ocean acoustic tomography has been successfully demonstrated in a variety of applications since its introduction. Some examples include mapping mesoscale midocean eddy fields (Cornuelle *et al.*, 1985), analysis of planetary waves (Chiu *et al.*, 1987), studying of ocean currents (DeFerrari *et al.*, 1986), and surface wave analysis (Lynch *et al.*, 1987). It has also been chosen as a monitoring tool as part of the Greenland Sea Project. Its application in the Greenland Sea is the impetus for this thesis.

The Greenland Sea is a well known contributor to world ocean ventilation. Several conceptual theories have been developed to describe the process, but direct observations of ventilation are scarce. The Greenland Sea Project was put forward by the Arctic

Ocean Sciences Board to gain understanding of the processes relevant to deep convection (Meincke, 1989).

B. THE GREENLAND SEA PROJECT

The Greenland Sea Project (GSP) is a five year (1987-1992), international scientific study to understand the large scale, long term interactions of air, sea, and ice in the Greenland Sea. The five key elements of the GSP are: (1) a study of air-sea-ice interaction, (2) a study of ocean ventilation, (3) a study of ocean circulation and mixing, (4) a study of atmospheric energetics, and (5) a study of biological processes. The role of ocean acoustic tomography is to assist in the studies of ocean ventilation and circulation. The array of transceiver moorings is designed to measure changes in the integrated properties of the Greenland Sea gyre through a winter cooling season and may also provide valuable information in measuring the response of the wind driven gyre to changes in the curl of the wind stress (Greenland Sea Science Planning Group, 1986).

A six transceiver array was successfully deployed in the Greenland Sea during September-October, 1988. Figure 1 depicts the planned deployment area and geometry of the array. The moorings were shifted slightly from their original planned location to accommodate for the rough bathymetry found at the original Mooring 3 site. Mooring 2 was redeployed due to leakage of some O-ring seals. The redeployed mooring is designated here as Mooring 2a. The geodic coordinates of the moorings, the source depths, and the receiver depths are given in Table 1. (Worchester and Howe, 1989).

C. THESIS OBJECTIVES

There are three basic objectives of this thesis. The first is to discuss the advantages and problems of predicting ray paths between array transceivers using an algorithm based on ray theory. The Greenland Sea offers an acoustic environment which, in conjunction with the array geometry, makes ray path determination challenging to model. Accurate ray path prediction is an essential element of establishing the "forward" problem. Chapter III contains our discussion on this topic.

The second objective is to develop an inversion code appropriate for application to Greenland Sea tomography data. We begin with an inversion code originated by Chiu and modified by Kao (1989). The code, or estimator, treats the ocean as a volume which has been subdivided into discrete boxes. The boxes have equal horizontal dimensions and the vertical layers of the ocean are equally spaced. An estimate of the unknown variable is calculated for each box. The estimator also treats the ocean as a statistically

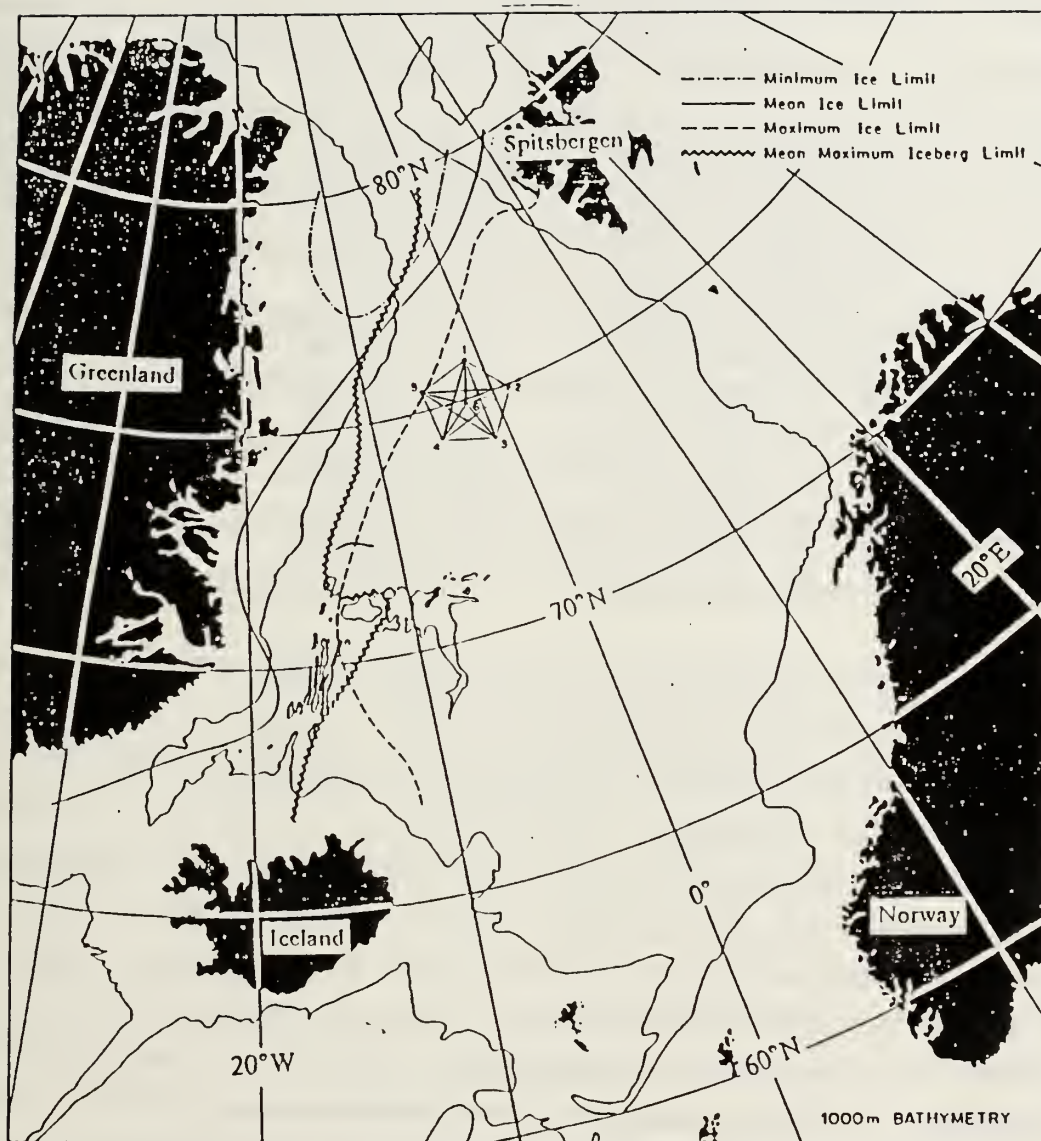


Figure 1. Planned Deployment Site of the Greenland Sea Tomography Array

Table 1. TRANSCEIVER LOCATIONS

Mooring	Lat-Long Position	X-Y Position (km)	Source Depth (m)	Receiver Depth (m)
1	75°58.08'N,001°50.00'W	154.790 220.317	99.7	150.4
2	75°03.69'N,000°40.25'E	224.683 119.080	94.0	144.7
2a	75°03.88'N,000°38.20'E	223.715 119.491	97.4	148.1
3	74°09.38'N,001°52.90'W	148.972 18.146	96.0	146.7
4	74°28.90'N,005°47.30'W	33.270 60.958	94.6	117.7
5	75°34.27'N,006°07.70'W	34.547 182.902	101.5	124.6
6	75°03.60'N,002°58.00'W	120.000 120.000	92.5	143.2

homogeneous volume. Therefore it expects variability (RMS values of the unknown variable) in any region of the ocean to be the same.

We have made two fundamental adjustments to the inversion code and discuss how they effect system performance. Our first adjustment is to vary the layer thickness so that there is a greater density of boxes in the region of interest. This adjustment allows for more detail in the region of interest without increasing the computational effort. Our second adjustment tells the estimator to expect a depth dependent variability distribution of the unknown variable. In this way, the estimator produces solutions which are more realistic statistically. The effects of the adjustments on system performance is evaluated by conducting inversions on computer simulated oceans with known statistical parameters. The results of these studies are also contained in Chapter III.

For convenience in coding, we use a Cartesian coordinate system. Based on ranges computed for the WGS84 spheroid (Worchester and Howe, 1989), we converted the latitude and longitude positions to an XY plane which closely approximates the geodic orientation. The plane is 240 km by 240 km and centered on Mooring 6. The XY coordinates are included in Table 1. Though there is some slight distortion in the overall shape of the array, the error between the geodic ranges and the model ranges is less than 15 meters along each path, as shown in Table 2 below.

Table 2. MOORING RANGES (KM) AND RANGE ERRORS (M): Ranges (above diagonal) are based on the WGS84 spheroid, range errors (below diagonal) are XY ranges minus spheroid ranges.

Mooring	1	2	2a	3	4	5	6
1	0	123.033	122.120	202.258	200.405	125.922	106.179
2	-13	0	1.039	126.177	200.057	200.576	104.701
2a	13	13	0	125.927	199.232	199.500	103.706
3	-3	-3	-1	0	123.367	200.594	105.896
4	1	-14	5	2	0	121.947	104.921
5	8	-14	13	-1	4	0	106.109
6	-1	-14	10	-2	-2	-1	0

Our third objective is to test the inversion code with observed data derived from the Greenland Sea tomographic array. The studies on system performance discussed earlier are conducted using computer simulated oceans with known characteristics. However, the simulated oceans are limited in the scope to which they can mimick the actual conditions found in the Greenland Sea. Using actual Greenland Sea travel time data is the only way to determine if the model response will be realistic. Currently there is a set of data derived from signals transmitted between Mooring 4 and Mooring 5 available for input into our model. The data set was processed by Woods Hole Oceanographic Institute (WHOI). Though this will not enable us to form significant conclusions about the array site from such a small data base, ingesting real data into our model is helpful in preparing the inversion code for the complete data set when it becomes available. Our results are discussed in Chapter IV.

To complete our study, we provide the following information. In Chapter II, we present an overview of the basis on which our system is developed. Here, the mathematical foundation of the tomographic "forward" and "inverse" problems is discussed. Then in Chapter V, we summarize our final conclusions and make recommendations for future improvements related to this work.

II. OVERVIEW OF ACOUSTIC TOMOGRAPHY PRINCIPLES

In general, the application of tomography to monitoring the ocean interior is done in two parts. In the "forward" problem, we establish a model describing the physical relationship between the observed data and the unknown variables which are to be estimated. We will cast the forward problem as a Fredholm Integral Equation of the First Kind in the form

$$d_i = \int_{\text{path}} g_i(s) f(s) ds + e_i \quad i = 1, 2, \dots, m \quad (2.1)$$

where d_i is the data accumulated along the i^{th} path, $g_i(s)$ is the data kernel which contains the physics and operates on the unknown, $f(s)$ is the unknown structure which is to be estimated, and e_i is the experimental noise accumulated along the i^{th} path.

The "inverse" problem is to determine a solution to the unknown structure which fits the data. An undetermined problem, one generally finds many solutions that fit the data and must choose an optimal solution based on some objective criteria. For the Greenland Sea transceiver array, the observed data are travel times of sound energy along reciprocal acoustic multipaths which "connect" sources and receivers. From these data, we can estimate both sound speed perturbations with respect to a reference ocean (density tomography), and ocean currents (current tomography).

A. THE FORWARD PROBLEM

Sound propagation in the ocean is a function of temperature, pressure, and salinity as well as a function of the current field. For the forward problem, we need to determine the acoustic multipaths which sound energy follows from source to receiver. To model these "eigenrays", we use an algorithm based on ray theory. Ray theory provides a simple physical description of the acoustic multipaths and the modeling equations are straightforward. We start with the eikonal equation,

$$|\nabla\Phi(x,y,z)|^2 = n(x,y,z)^2 \quad (2.2)$$

where Φ is the acoustic phase defining a wave front and n is the index of refraction. Following the example of Ziomek (1985), we neglect horizontal refraction so that the predicted ray paths lie on a vertical plane passing through the source and receiver.

Following the derivation used by Kao (1989), and treating the reference ocean as a motionless medium, we arrive at the key equation for modeling ray paths in the Greenland Sea.

$$z = z_o \pm \int_{R_o}^R \sqrt{\left(\frac{n(z)}{\cos \theta_o}\right)^2 - 1} dR \quad (2.3)$$

where z is the depth of the ray at range R , θ is the ray path angle with respect to the horizontal, and the subscript o indicates conditions at the acoustic source.

The speed of the wave front through the true ocean is affected by both the sound speed and current structure along the path. We express this as

$$\frac{ds}{dT} = c(x,y,z,t) + \vec{V}(x,y,z,t) \cdot \hat{s} \quad (2.4)$$

where c is sound speed, \vec{V} is the ocean current field, and \hat{s} is a unit vector tangent to the ray path, s , and pointed in the direction of sound energy propagation. From Equation (2.4), we can determine the sound travel time along an eigenray path.

$$T = \int_{\text{path}} \left(\frac{1}{c + \vec{V} \cdot \hat{s}} \right) ds \quad (2.5)$$

We further separate c into the sum of sound speed in a reference ocean and sound speed perturbations with respect to this reference,

$$c = c_o + \delta c \quad (2.6)$$

Travel time can also be separated into the sum of travel time along an eigenray in a reference ocean and the perturbation in travel time due to effects in the ocean not represented by the reference conditions,

$$T = T_o + \delta T \quad (2.7)$$

Substituting Equations (2.6) and (2.7) into Equation (2.5), we have

$$T_o + \delta T = \int_{\text{path}} \frac{1}{c_o} \left(\frac{1}{1 + \frac{\delta c + \vec{V} \cdot \hat{s}}{c_o}} \right) ds \quad (2.8)$$

Under the mild restriction that $|\delta c + \vec{V} \cdot \hat{s}| \ll |c_o|$, we can neglect the higher order terms of a Taylor series expansion of the term in parenthesis and arrive at

$$T_o + \delta T \simeq \int_{\text{path}} \frac{1}{c_o} \left(1 - \frac{\delta c + \vec{V} \cdot \hat{s}}{c_o} \right) ds \quad (2.9)$$

In density tomography, which uses one way travel times, the effect of ocean currents is much smaller than the effects of temperature, pressure, and salinity, i.e.

$|\vec{V} \cdot \hat{s}| \ll |\delta c|$. Since we have defined $T_o = \int_{\text{path}} \frac{1}{c_o} ds$, Equation (2.9) reduces to the linearized form

$$\delta T = \int_{\text{path}} \left(\frac{-1}{c_o^2} \right) (\delta c) ds \quad (2.10)$$

In current tomography, we must consider reciprocal paths. The effects of temperature, pressure, and salinity are the same in either direction whereas the effects of the current field will be opposite under these circumstances. Therefore, imbedded information about the currents may be extracted by subtracting the two reciprocal path equations.

Consider the the travel time for sound along a path indicated by \Rightarrow calculated from Equation (2.9),

$$T_o + \delta T^{\Rightarrow} = \int_{\text{path}} \frac{1}{c_o} \left(1 - \frac{\delta c + \vec{V} \cdot \hat{s}^{\Rightarrow}}{c_o} \right) ds \quad (2.11)$$

and for its reciprocal path indicated by \Leftarrow ,

$$T_o + \delta T^{\Leftarrow} = \int_{\text{path}} \frac{1}{c_o} \left(1 - \frac{\delta c + \vec{V} \cdot \hat{s}^{\Leftarrow}}{c_o} \right) ds \quad (2.12)$$

Since $\vec{V} \cdot \hat{s}^{\Leftarrow} = -\vec{V} \cdot \hat{s}^{\Rightarrow}$ at all points on the paths, subtracting Equation (2.12) from Equation (2.11) yields a linearized expression for current,

$$\left(\frac{\delta T^{\Rightarrow} - \delta T^{\Leftarrow}}{2} \right) = \int_{\text{path}} \left(\frac{-1}{c_o^2} \right) (\vec{V} \cdot \hat{s}^{\Rightarrow}) ds \quad (2.13)$$

Thus far, the forward model has treated travel time data only as noise free measurements. In practice, experimental noise corrupts the signal and contributes to the error in the estimates. Factors such as tidal forces which cause displacement of transceiver elements and internal waves are sources of experimental noise. Signal processing is used to minimize these effects. Details of signal processing techniques used for ocean tomography can be found in Spindel (1985).

Including experimental noise in our model, we now have expressions which relate the unknown variables to practical, observable data. For density tomography, we have

$$\delta T = \int_{\text{path}} \left(\frac{-1}{c_o^2} \right) (\delta c) ds + e_{\delta c} \quad (2.14)$$

and for current tomography, we have

$$\left(\frac{\delta T^{\Rightarrow} - \delta T^{\Leftarrow}}{2} \right) = \int_{\text{path}} \left(\frac{-1}{c_o^2} \right) (\vec{V} \cdot \hat{s}) ds + e_v \quad (2.15)$$

The similarity of the data kernels, which contain the physics of the model, shows the close relationship between the two areas of tomography.

B. THE INVERSE PROBLEM

Once the forward problem has been established, we search for unknown structures which fit the observed data. Since we cannot sufficiently sample the ocean to have a complete set of independent data, the problem is underdetermined, with an infinite number of possible solutions that will fit the data. To reach a unique solution, we must devise an estimator which imposes additional constraints on the system. Choosing an estimator based on the Gauss-Markoff Theorem allows the use of statistical information to evaluate system performance.

1. The Estimator

We approximate the continuous system in a discretized form. This allows us to cast the problem into matrix algebra for straightforward implementation of the estimator in a numerical computer. Applying the Gauss-Markoff Theorem (Liebelt, 1967) and following the works of Cornuelle *et al.* (1985) and Chiu *et al.* (1987), our criterion for the "best" solution of the unknown structure is one that is linear with the data and has minimal mean square error with respect to the true solution. Additional constraints on the system are imposed through the specification of an *a priori* covariance matrix.

Posing the forward problem in discretized form, we have

$$\underline{d} = \mathbf{A}\underline{f} + \underline{e} \quad (2.16)$$

where the m dimensional column vector, \underline{d} , contains the data derived from travel times of m resolvable eigenrays. The n dimensional column vector, \underline{f} , is the unknown structure to be estimated. The ocean has been divided into n discrete boxes, within each the unknown variable, δc or \bar{V} , is assumed to be constant. In our treatment, the discrete boxes have equal dimensions in the horizontal plane, forming squares. However, the vertical dimension varies with depth, forming uniform layers of different thicknesses. The experimental noise, \underline{e} , which contaminates the data along each ray path, is also m dimensional. The linear operator matrix, \mathbf{A} , has $m \times n$ dimensions. The rows of the operator matrix are analogous to a set of data kernels of the continuous case. They contain the physics which relates the data and unknown fields.

From the Gauss-Markoff Theorem, the optimal estimate of an unknown parameter can be calculated from

$$\hat{\underline{f}} = \mathbf{C}_e \mathbf{A}^T \mathbf{C}_e^{-1} \underline{d} \quad (2.17)$$

where the covariance matrix of the total error, \underline{e} , of the estimate is

$$\mathbf{C}_\epsilon = \mathbf{C}_f - (\mathbf{C}_f \mathbf{A}^T)(\mathbf{A} \mathbf{C}_f \mathbf{A}^T + \mathbf{C}_\epsilon)^{-1}(\mathbf{C}_f \mathbf{A}^T)^T \quad (2.18)$$

The diagonal elements of \mathbf{C}_ϵ are the minimum mean square errors of the estimate. \mathbf{C}_ϵ is the covariance matrix of experimental noise, which we assume is known, and \mathbf{C}_f is the covariance matrix of the unknown variable. It is through \mathbf{C}_f that we insert *a priori* information in the estimator. To reach an optimal solution, we assume the unknown fields have Gaussian distributions and are statistically homogeneous throughout each layer. We express these conditions through a covariance function, C_f , which is cast into matrix form as \mathbf{C}_f . The covariance function is expressed as,

$$C_f = \sigma(x', y', z') \sigma(x'', y'', z'') \exp \left\{ - \left[\left(\frac{\Delta x}{L_x} \right)^2 + \left(\frac{\Delta y}{L_y} \right)^2 + \left(\frac{\Delta z}{L_z} \right)^2 \right] \right\} \quad (2.19)$$

where the separation of two points in each dimension is given as $\Delta x = x'' - x'$, $\Delta y = y'' - y'$, and $\Delta z = z'' - z'$, respectively. The dimensional correlational lengths, L_x , L_y , and L_z tell the estimator how well information at one point relates to surrounding points in the system. It is optimal to use the true correlation lengths, but the true values may not be well known. To avoid overconstraining the system, i.e. to avoid correlating information which is not truly correlated, we can use conservatively small values of L_x , L_y , and L_z . We characterize the vertical variability distribution of the unknown field through σ , which is treated by the estimator as an exponentially decaying function with depth, parameterized by a surface value and an e -folding depth. In each layer, an average value based on this curve is used. With *a priori* knowledge in place, the inversion code can generate a unique least mean square error solution from observed data as well as error bars and system resolution measures.

2. Measurement of Error

The total error in the estimate can be cast as two statistically independent terms; bias, $\underline{b} = \langle \hat{f} \rangle - f$, and random error, $\Delta \hat{f} = \hat{f} - \langle \hat{f} \rangle$. The covariance of error is simply the sum of its components,

$$\mathbf{C}_\epsilon = \langle \underline{b} \underline{b}^T \rangle + \mathbf{C}_{\Delta \hat{f}} \quad (2.20)$$

where

$$\mathbf{C}_{\Delta \hat{f}} = \mathbf{C}_\epsilon \mathbf{A}^T \mathbf{C}_\epsilon^{-1} \mathbf{A} \mathbf{C}_\epsilon \quad (2.21)$$

Following Chiu *et al.* (1987) and Wiggins (1972), we apply a powerful tool called singular value decomposition of matrices. The linear operator matrix, \mathbf{A} , is scaled and factorized into a diagonal matrix of eigenvalues, Λ , and two matrices of associated eigenvectors, \mathbf{U} and \mathbf{V} such that,

$$\mathbf{C}_\epsilon^{-\frac{1}{2}} \mathbf{A} \mathbf{C}_f^{\frac{1}{2}} = \mathbf{U} \Lambda \mathbf{V}^T \quad (2.22)$$

Each diagonal element of Λ , λ_i , has two associated eigenvectors, \mathbf{u}_i and \mathbf{v}_i , which are the i^{th} columns of \mathbf{U} and \mathbf{V} , respectively. The eigenvectors within \mathbf{U} and \mathbf{V} are sets of orthogonal basis vectors in the data space and unknown parameter space, respectively.

Applying matrix decomposition as in Chiu *et al.* (1987), we now write the covariances of total error and random error as

$$\mathbf{C}_\epsilon = \mathbf{C}_f^{\frac{1}{2}} [\mathbf{I} - \mathbf{V} \Lambda (\mathbf{I} + \Lambda^2)^{-1} \Lambda \mathbf{V}^T] \mathbf{C}_f^{\frac{1}{2}} \quad (2.23)$$

and

$$\mathbf{C}_{\Delta f}^{\wedge} = \mathbf{C}_f^{\frac{1}{2}} [\mathbf{V} (\mathbf{I} + \Lambda^2)^{-1} \Lambda^2 (\mathbf{I} + \Lambda^2)^{-1} \mathbf{V}^T] \mathbf{C}_f^{\frac{1}{2}} \quad (2.24)$$

where \mathbf{I} is an $n \times n$ identity matrix. We derive an expression for bias by taking the extreme case where all eigenvalues approach infinity so that $\mathbf{C}_{\Delta f}^{\wedge}$ approaches zero. From Equation (2.23) we have,

$$\langle \underline{b} \underline{b}^T \rangle = \mathbf{C}_f^{\frac{1}{2}} (\mathbf{I} - \mathbf{V} \mathbf{V}^T) \mathbf{C}_f^{\frac{1}{2}}. \quad (2.25)$$

3. Measurement of Resolution

Besides a measure of error, we also evaluate system performance through its ability to resolve ocean features. Continuing with singular value decomposition of matrices, we obtain an expression for the optimal estimate in terms of eigenvalues,

$$\mathbf{C}_f^{-\frac{1}{2}} \hat{\mathbf{f}} = \sum_{i=1}^k \frac{\lambda_i}{\lambda_i^2 + 1} (\mathbf{u}_i^T \mathbf{C}_\epsilon^{-\frac{1}{2}} \underline{d}) \mathbf{v}_i \quad (2.26)$$

where k is the number of non-zero eigenvalues. Equation (2.26) shows the solution is a weighted sum of eigenvectors where the eigenvalues control the weighting. The ex-

pression in parenthesis represents the components of the data vector which has been expanded into a linear combination of weighted eigenvectors. As demonstrated by Chiu *et al.* (1987), the λ_i^2 values are analagous to signal-to-noise ratios for each component of the expanded data vector. For $\lambda_i^2 \gg 1$, signal dominates noise in that particular component, and the reverse is true for $\lambda_i^2 \ll 1$. From Equation (2.26) we see that the effect of noise on the estimate is minimized by downweighting those components associated with high noise levels.

We now define the resolution matrix, \mathbf{R} , which has $n \times n$ dimensions,

$$\mathbf{R} \equiv \mathbf{V}\mathbf{\Lambda}(\mathbf{I} + \mathbf{\Lambda}^2)^{-1}\mathbf{\Lambda}\mathbf{V}^T \quad (2.27)$$

The i^{th} row of \mathbf{R} is the resolution kernel of the i^{th} box in the discretized ocean. Substituting into Equation (2.23), we get

$$\mathbf{C}_\epsilon = \mathbf{C}_f^{\frac{1}{2}}(\mathbf{I} - \mathbf{R})\mathbf{C}_f^{\frac{1}{2}} \quad (2.28)$$

Ideally, if the resolution matrix is an identity matrix, the system has no error. In the limit, as we approach the continuous case with complete and noise free data, the resolution kernels approach delta functions and the system would be perfectly resolved. In practice, however, the resolution kernels have side lobes and amplitudes less than unity along the diagonal. In Equation (2.28), the relationship between resolution and error is linear. Therefore, we may use the resolution kernel peak value as a simple measure of local resolution.

Another measure of system performance is a measure of the size of features that can be adequately resolved by the system. Chiu *et al.* (1987) has defined scale measurements called the horizontal and vertical minimum resolution lengths, H and V , respectively. Each represents the distance in the respective dimension within which one half of the total energy of the i^{th} resolution kernel is confined under noise free conditions. They are calculated from the following expressions,

$$H_x(x', y', z') = 2 \sqrt{\sum_{j=1}^n \Delta x^2 \frac{r_j^2(x'', y'', z'')}{E_i}} \quad (2.29)$$

$$H_y(x', y', z') = 2 \sqrt{\sum_{j=1}^n \Delta y^2 \frac{r_j^2(x'', y'', z'')}{E_i}} \quad (2.30)$$

$$I'(x', y', z') = 2 \sqrt{\sum_{j=1}^n \Delta z^2 \frac{r_j^2(x'', y'', z'')}{E_i}} \quad (2.31)$$

where

$$E_i = \sum_{j=1}^n r_j^2 \quad (2.32)$$

is the total energy of the i^{th} resolution kernel and r_j^2 is the energy contained in the j^{th} element of the i^{th} resolution kernel. In three dimensional space, the center of the box associated with the i^{th} diagonal element of \mathbf{R} is located at (x', y', z') , and the center of the box associated with the j^{th} element of the i^{th} resolution kernel is located at (x'', y'', z'') . Thus, Δx , Δy , and Δz are the separation distances in each dimension, respectively, between these locations. A significant strength of measuring system performance this way is that the RMS error and resolution do not depend on the available data. Instead, error and resolution can be determined once the eigenray paths through the discretized ocean are determined and the covariances of the unknown variable and random error are known.

III. EIGENRAY PREDICTION AND INVERSION CODE DEVELOPMENT

In this chapter, we first discuss eigenray path prediction for the Greenland Sea array. Eigenrays are paths of acoustic signals extending between sources and receivers. Accurate eigenray paths are needed to establish the forward problem. Errors in ray positioning and travel time calculations introduce errors to the inverse solution. We then discuss the modifications that have been made to the inversion code and their effects on system performance.

A. EIGENRAY PATH PREDICTION

The construction of the linear operator is dependent on ray path information. Knowing the amount of path length a ray has in each box is essential for the estimator to determine the distribution of unknown structures. Collectively, these structures result in a travel time perturbation datum as an acoustic signal passes from source to receiver. We use an algorithm based on ray theory to predict eigenray paths since ray theory provides a simple physical description and the equations used in modeling are straightforward.

The ray trace algorithm is a fourth order Runge-Kutta numerical integration technique applied to Equation (2.4). The depth of each ray is calculated at 1000 range steps. Details of the fourth order Runge-Kutta method are given in Gerald (1989). As the ray reaches significant points where the vertical sense of motion reverses, i.e. turning points and surface reflections, the sign of the second term of Equation (3.1) reverses. (Since we have not included bottom interacting eigenrays in our forward problem, we will not consider bottom reflections in our discussion here.) The Runge-Kutta method cannot be applied through a step containing a significant point. Therefore, in the vicinity of a turning point or a surface reflection, we apply a method which assumes a locally constant sound speed gradient at depths near the significant point. Under constant gradient conditions, the ray path is circular. From Ugincius(1970), we have an expression for curvature of the ray path,

$$\kappa = \frac{1}{c} [g_z(v - \cos \theta) + g_v(2 \cos \theta v - 1)] \quad (3.1)$$

where g_c is the sound speed gradient and g is the gradient of the medium speed. The radius of curvature, \mathcal{R} , is just the reciprocal of κ . Since we use a motionless reference ocean in the forward problem, the expression for the radius of curvature simplifies to

$$\mathcal{R} = - \frac{c}{g_c \cos \theta} \quad (3.2)$$

which shows \mathcal{R} is inversely related to the sound speed gradient with smaller radii resulting from stronger gradients. In turning point cases, the ray is projected through the step containing the point at a constant \mathcal{R} , then the Runge-Kutta integration continues. In surface reflection cases, the ray is projected to the surface and continues downward at the same \mathcal{R} , however, for the downward path, the center of the circle for \mathcal{R} is symmetrically relocated about a vertical line extended through the point of reflection. As in the turning point case, the Runge-Kutta integration continues at the completion of the step until the next significant point is reached. Figure 2 shows examples of ray tracing through steps containing significant points.

To establish the forward problem, a reference ocean must be chosen. The associated sound speed profile needs to closely approximate the true conditions expected in the Greenland Sea so that model predicted rays can be associated with the data from the tomographic array. When the transceiver moorings were deployed, sound speed profiles were generated at each site from CTD data. The profiles indicate a thin, warm layer of relatively fresh water lies above a sharp density gradient. The sharp gradient extends 20-50 m below the top layer. Below the gradient, the water column approaches adiabatic conditions at 500-1000 m, and is essentially adiabatic below 1000 m. For simplicity in modeling, we treat the sound speed profile as a function of depth only. The reference profile is based on a profile taken near the center of the array. The profile was taken at the beginning of the data collection period on yearday 264 near Mooring 6 and is shown in Figure 3. Yearday 1 is defined as 01 Jan 88 throughout this work. The presence of the sharp and rapidly changing gradients in this profile near the surface in conjunction with the source and receiver locations proves to be challenging for our ray tracing algorithm.

Under certain circumstances, small differences in sound speed profiles can result in important output differences from our ray tracing algorithm. The top 40 meters of two similar profiles with slightly different layer depths are shown in Figure 4. From 40 meters to the bottom at 3000 meters, the profiles are identical. Either profile is representative of the conditions near Mooring 6. We have depicted the deeper layer (DL) case

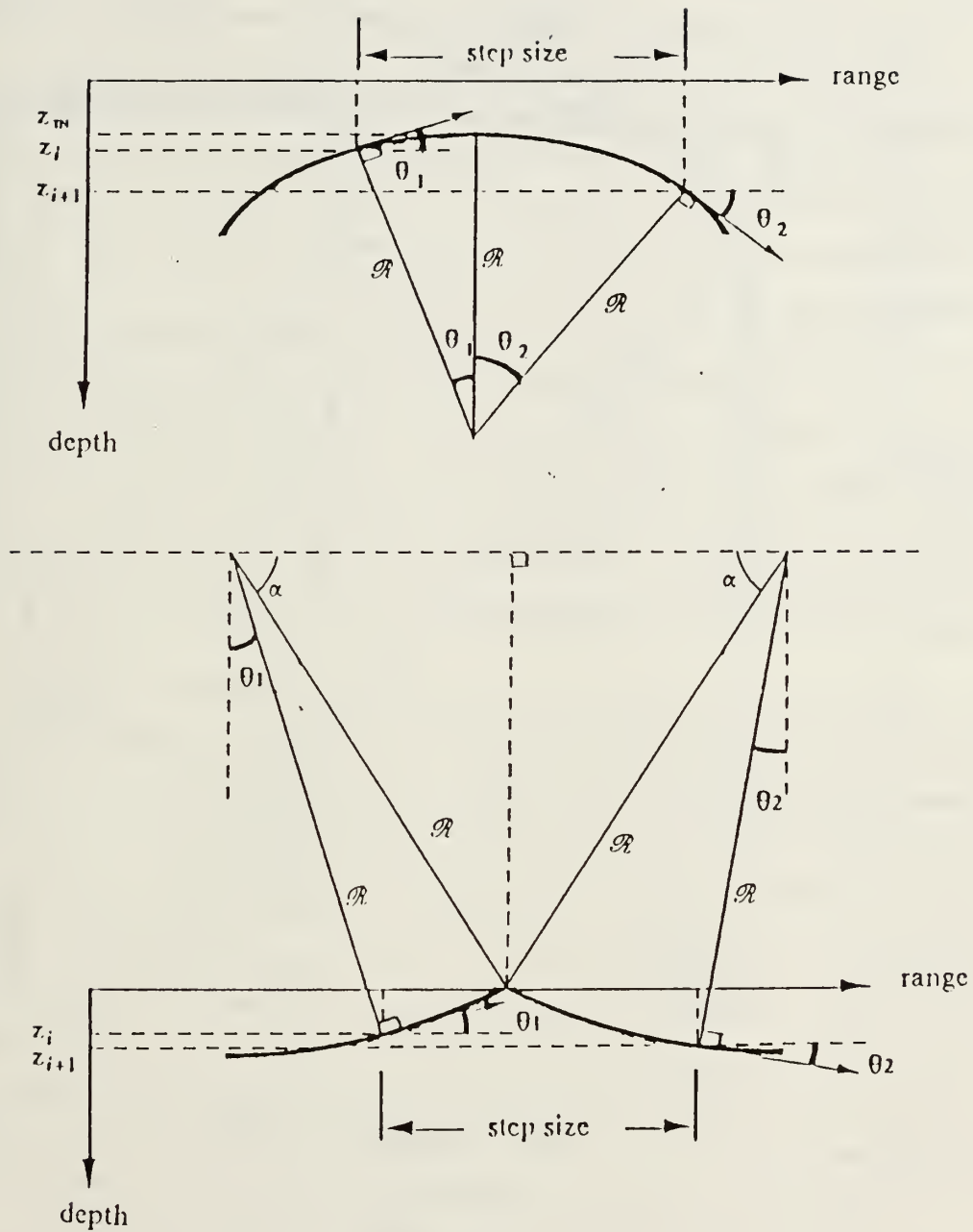


Figure 2. Path Segment Geometry Through Significant Points: a) Turning point example. b) Surface reflection example.

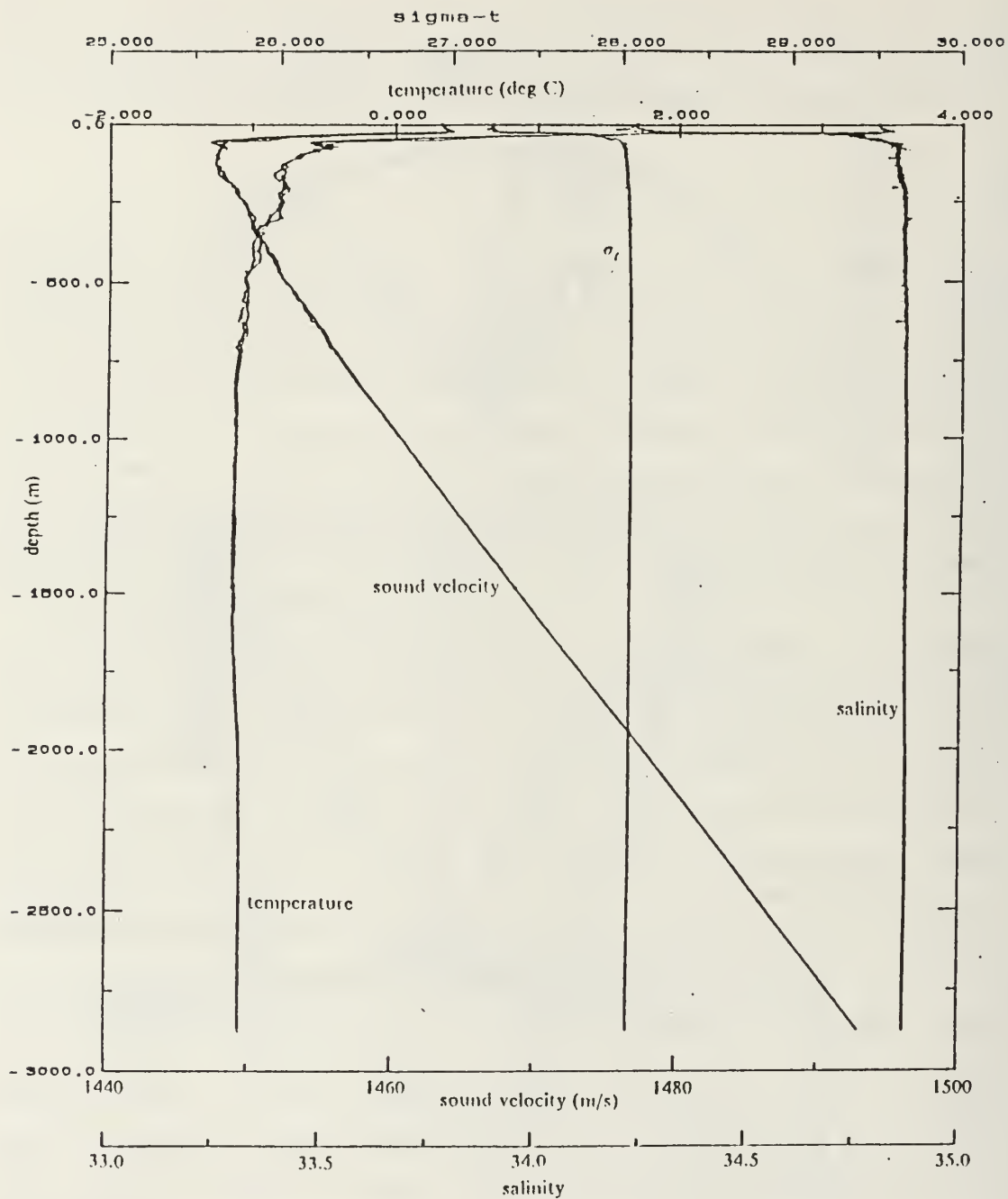


Figure 3. CTD Data at Mooring 6 on Yearday 264: From Worchester and Howe (1989). Yearday 1 = 01/01/88.

as a possible result of entrainment of five meters of the sharp gradient found in the shallower layer (SL) case by mechanical means.

Typically, eigenrays occur in bundles of four distinct rays due to the near surface location of the transceiver elements and near half channel conditions of the Greenland Sea. Two rays in the bundle are launched downward within a few tenths of a degree of each other. The deeper ray arrives at the receiver from below while the shallower ray reflects off the surface just prior to reaching the receiver, then arrives from above. The other two rays in the bundle are launched upward at nearly the same magnitude launch angle as the downward rays. Again, the ray launched at the steeper angle arrives from below while the shallower ray reflects just before the receiver and arrives from above. Since the magnitudes of the receiving angles are nearly the same for all four rays and the bundles are several degrees apart, the bundles are identified by a nominal receiving angles. To identify ray paths as eigenrays, our algorithm uses a tolerance of ± 100 meters vertical displacement from the receiver as a threshold. This threshold usually allows us to identify all four eigenrays at some nominal receiving angle using 0.1° separation in launch angle.

Eigenray paths between Mooring 4 and Mooring 5 with launch angles $\pm \theta$ are shown in Figure 5 where $7^\circ \leq \theta \leq 14^\circ$. Figure 5a shows paths based on the DL profile. The SL case is shown in Figure 5b. With only a five meter difference in layer depth, several of the eigenrays predicted for the DL case are not predicted for the SL case. The rays of the SL case reach the top layer at lower angles and continue in the layer for longer ranges before returning to the lower ocean. The rays of the DL case reach the surface layer at higher angles and have less path in the high speed water, which results in a significantly different path from the SL case. Rays leaving a source at the same launch angle, $\theta = -9.03^\circ$, in the two different environments are shown in Figure 5c. In the DL case, the ray is projected to pass less than 100 m from the receiver and is considered to be an eigenray. In the SL case, a ray with the same launch angle is projected below the receiver by over 200 meters.

The selection of predicted eigenray paths used for the inversion of data from the Greenland Sea depends on which paths best match the signal processing results of the array data. The data we have received for paths between Mooring 4 and Mooring 5 indicate, there are four distinct paths at a nominal receiving angle of $\pm 13^\circ$, four paths at $\pm 10^\circ$, and the slowest arrival which occurs near 0° . Therefore we have chosen to include the eight steepest eigenrays predicted in the DL case for our inversion of Greenland Sea data. These rays are at nominal angles that best match the true ocean

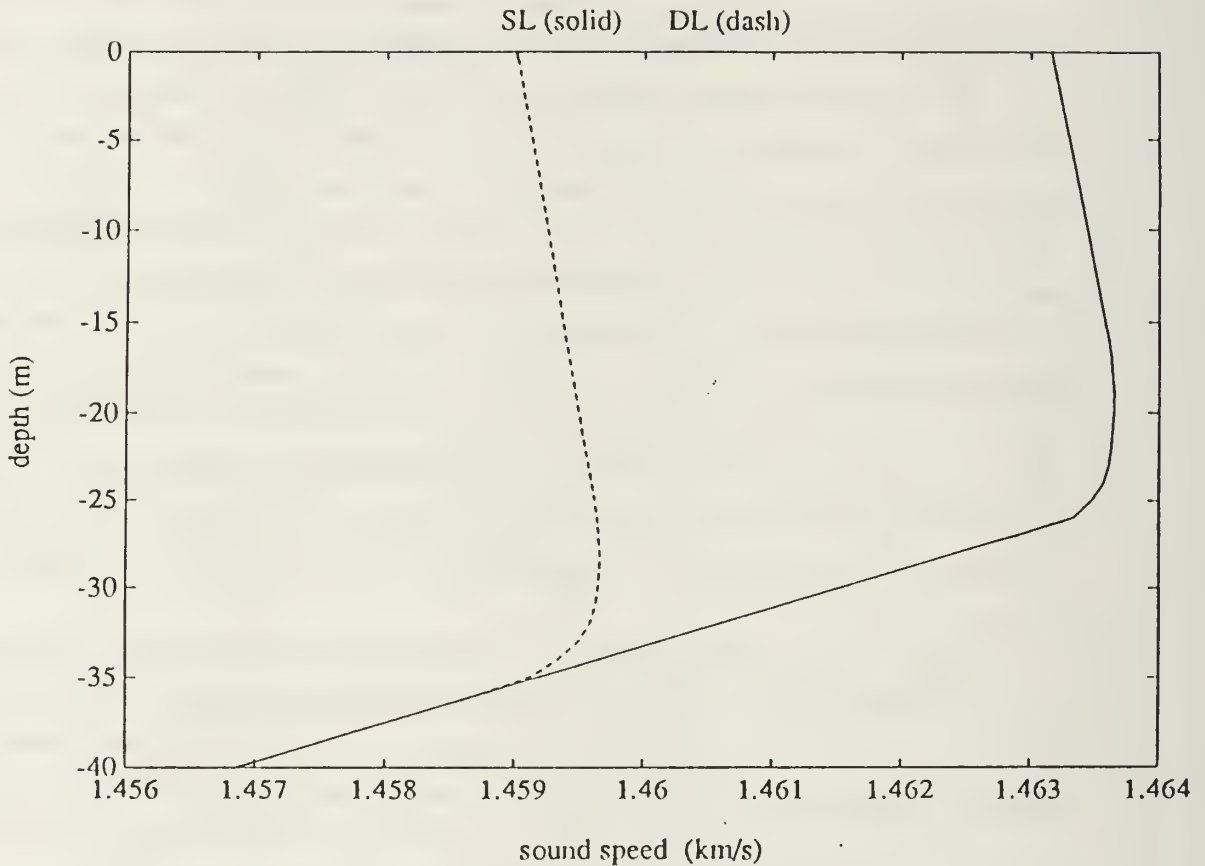


Figure 4. Near Surface Sound Speed Profiles: Both profiles are representative of the profile at Mooring 6.

data. In Chapter IV, we will continue our discussion of the inversion of data from the deployed array.

The presence of strong and rapidly changing gradients in our reference sound speed profile causes another problem for our ray tracing algorithm. At relatively shallow launch angles, typically with θ between $\pm 5^\circ$, the algorithm fails while projecting the ray through a turning point in the strong, near surface gradient. The exact cause of failure needs to be fully investigated, but a preliminary look indicates a higher degree of numerical accuracy is required and ray behavior in the vicinity of rapidly changing gradi-

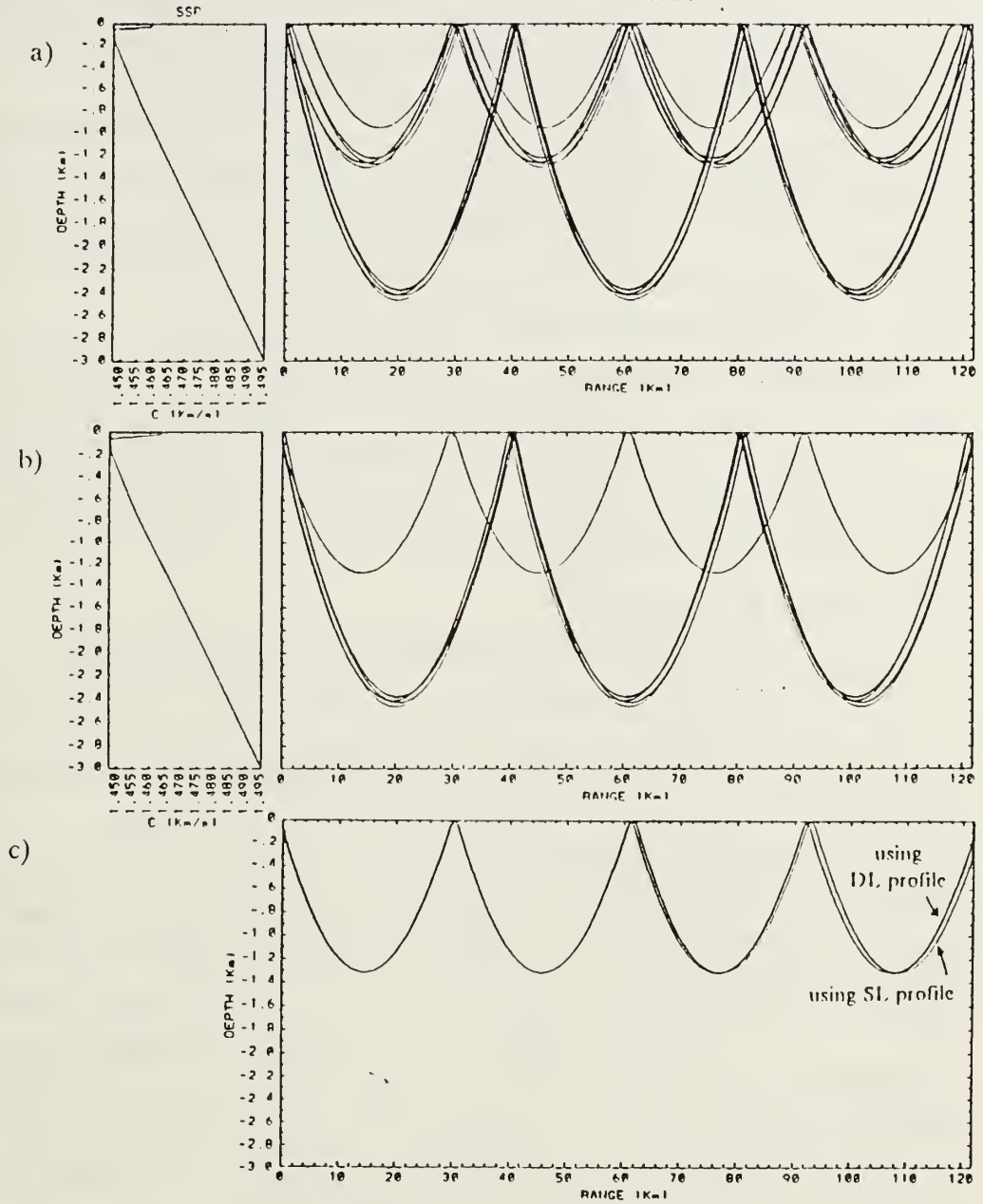


Figure 5. Sound Speed Effects on Eigenray Paths: Launch angles: $7^\circ \leq \theta \leq 14^\circ$
a) DL case eigenrays. b) SL case eigenrays. c) Comparison of rays launched at $\theta = -9.03^\circ$ using DL and SL profiles.

ents is not accurately depicted. Based on these results, we can expect the accuracy of the ray tracing output to degrade at shallower launch angles, in the presence of high sound speed gradients, and in the presence of rapidly changing gradients.

In conducting our studies involving the entire array, we select 101 eigenrays along the 15 paths between moorings shown in Figure 6. The geometry of the array results in three general types of ray patterns: 1) Short paths between outer transceivers, 2) long paths between outer transceivers, and 3) paths between the outer transceivers and the center transceiver. An example of each is provided in Figure 7.

More eigenrays were predicted, but not used for three reasons. First, we have less confidence in the accuracy of ray traces of shallow eigenrays. Also, initial results indicate that distinct travel time arrivals for shallower ray paths may not be available, and finally, we feel using these 101 eigenrays in our 500 box discretized ocean model is sufficient to determine sensitivity effects without taxing the limits of the microcomputer used to conduct the experiments.

B. VERTICAL LAYERS AND RMS VARIABILITY DISTRIBUTION

The estimator arrives at a more realistic solution if *a priori* information guides it towards a statistically sensible solution. Since we generally expect to find more strongly defined signatures of the unknown structures in the upper portion of the ocean volume, we wish to focus the resolving capability of the estimator in this region. To accomplish this, we make two adjustments to the inversion code. We vary the thickness of the vertical layers rather than using equally spaced layers and we describe the vertical variability distribution of unknown variable to the estimator through the variable's covariance matrix. Varying the thickness of layers allows us to use more boxes of smaller size to describe the region of greater variability without increasing the number of discrete boxes. Thus, the computational effort to generate a solution is not significantly affected.

To show the effects of our adjustments on model performance, we use an ocean volume which is 240 km x 240 km in the horizontal, and 3 km deep. The horizontal dimensions are evenly divided into ten 24 km segments. There are five vertical layers. Starting at the surface, the layers are 100 m, 200 m, 450 m, 750 m, and 1500 m thick, respectively. Because of the uneven vertical spacing, the lower boxes generally contain a larger portion of eigenray paths than if the model used evenly spaced layers. As a result, the estimator places greater weight on the lower boxes when generating solutions. Figure 8 depicts the resolution kernel peak values along a vertical slice using variable thickness layers (VTL). Figure 9 shows the resolution kernel peak values for an equally

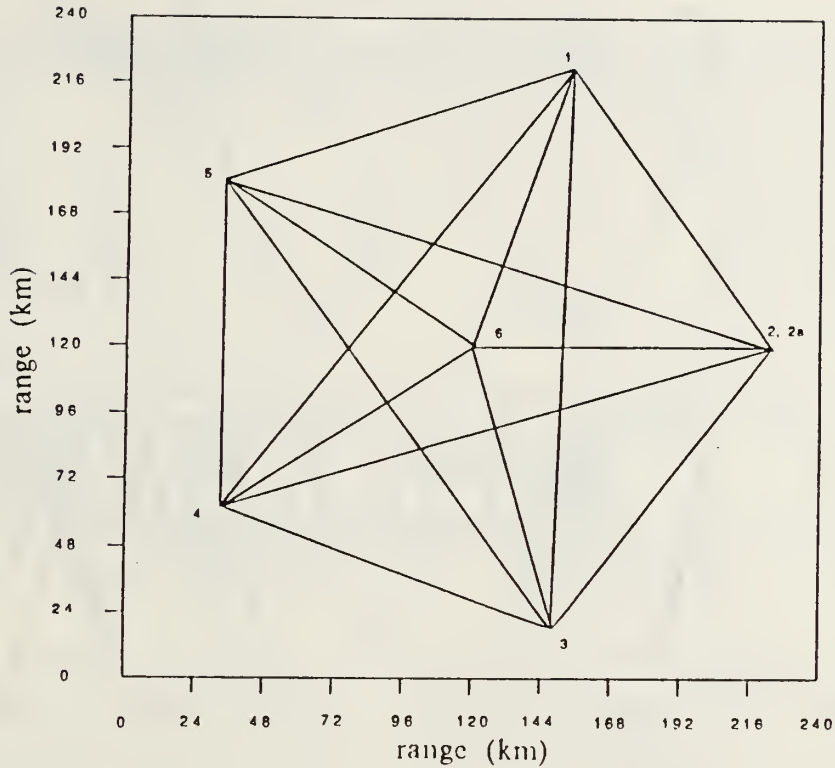


Figure 6. Plan View of Array Geometry

spaced (EQS) discretized ocean having layers of 600 m each. Both cases use the same eigenray paths and the slices are taken parallel to the y-axis along the seventh increment in x , that is for $144\text{km} \leq x \leq 168\text{km}$ (see Figure 6). These slices essentially parallel the ray paths between Mooring 1 and Mooring 3. Both estimators assume a constant RMS sound speed perturbation equal to 2 m/s throughout the ocean.

The resolution kernel peak values are a measure of the resolving capability of the estimator at a particular location. They reflect the way the estimator views the data collection process as an acoustic signal travels along an eigenray path. In the EQS approach, the estimator assumes that a greater portion of the signal was accumulated above 1000 m since most of the eigenray paths are found in this region, however, this approach uses fewer boxes to describe the structure of the upper ocean. The VTL approach, in contrast, uses more boxes to describe the upper region and thus gives more detail on the solution there. However, the VTL approach also shifts resolution towards the lower ocean where the system has long paths passing through the thick lowest layer

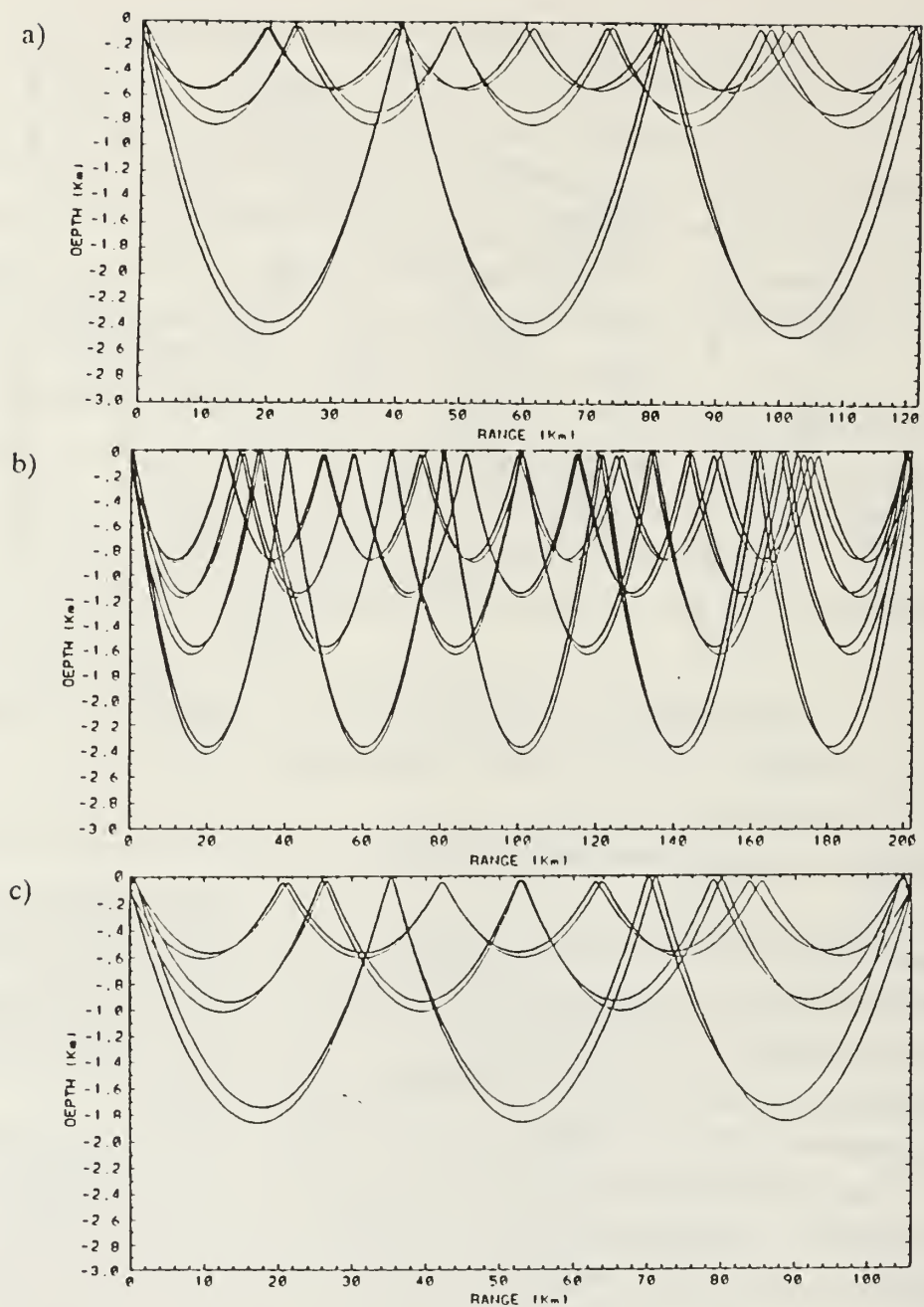


Figure 7. Eigenray Paths along Vertical Slices: a) Paths between Moorings 1 and 2a. b) Paths between Moorings 1 and 3. c) Paths between Moorings 1 and 6.

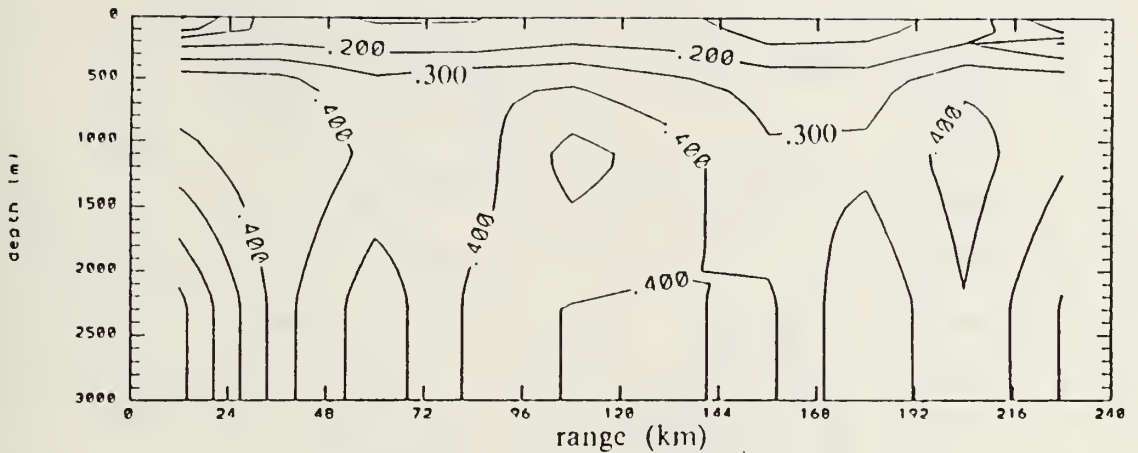


Figure 8. Resolution Kernel Peak Values (VTL approach): A value of 1.0 implies a box is well resolved.

of boxes. The increased detail on system performance in the upper ocean and the increased number of estimated points provided by using smaller boxes are characteristics of the VTL approach which we wish to exploit since we expect greater variability in this region. At the same time, we wish to limit the effect of shifting system resolution towards the lower ocean.

In the oceans described above, the estimators do not expect greater variability in the unknown field in any particular region. This allows the estimator the freedom to generate solutions which show features of unusually high intensity in regions where we realistically do not expect them. This occurs if the solution meets the requirements of the estimator, that is, it fits the data and provides the least mean square error. We can inform the estimator to anticipate greater RMS values of the unknown field in the upper ocean through the covariance of the estimate. In this way the estimator expects little travel time perturbation will accumulate in the acoustic wave as it passes through the deeper ocean layers and greater variability is encountered in the upper regions. As a result, the resolution kernel peak values show an upward shift in model resolution, offsetting the downward shift caused by varying the thickness of layers. In Figure 10, we show a vertical slice of the results of using the VTL approach with a vertical dependent variability function. The vertical slice is the same as that used in Figures 8 and 9. In our example, the RMS sound speed perturbation is modeled as an exponentially decay-

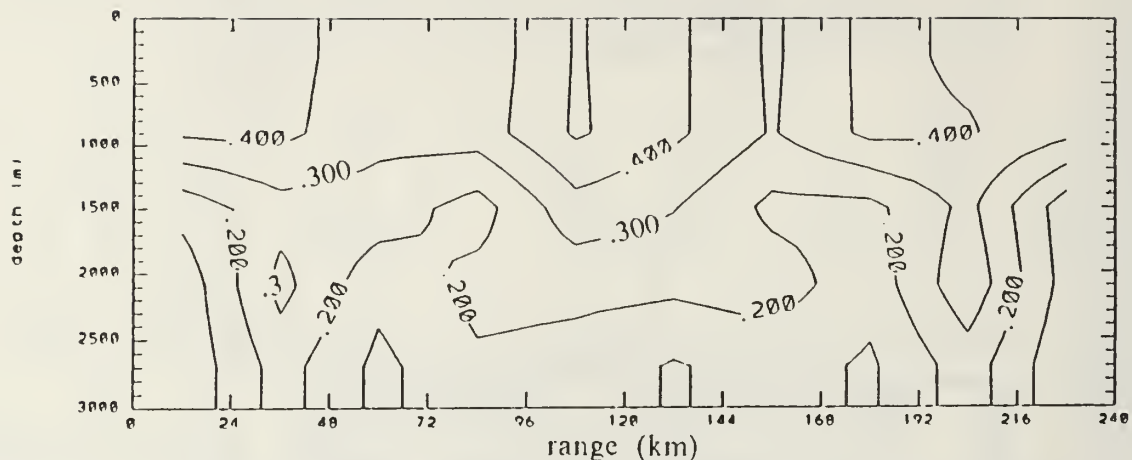


Figure 9. Resolution Kernel Peak Values (EQS approach): A value of 1.0 implies a box is well resolved.

ing function with depth. An average value is then calculated for each layer. For the example shown in Figure 10, we have characterized the function by a surface RMS value of 6 m/s and an e -folding depth of 1000 m. The average value for the entire ocean using this function is 1.9 m/s, which closely approximates the 2 m/s RMS δc used for the example shown in Figure 9.

Though we show an improvement in resolution in the upper region of the ocean, it does not come without cost. As we improve resolution in a region, we also allow more random noise to pass through the estimator. The effect can be seen in the standard deviation of the estimate, and thus a less reliable solution. The balance of higher resolution and lower random error is a choice which must be decided on the basis of resolvable eigenrays paths, array geometry, and the amount of experimental noise that can be expected. Generally, we wish to increase system resolution with a minimal increase in standard deviation of the estimate. Figure 11 shows the associated upward shift in standard deviation of the estimate corresponding to an upward shift in system resolution. The RMS δc distribution used for the examples shown in Figures 11a and 11b are the same as that used for examples shown in Figures 9 and 10, respectively. Typically, bias tends to dominate the total error of the system and the increase in random error is less important.

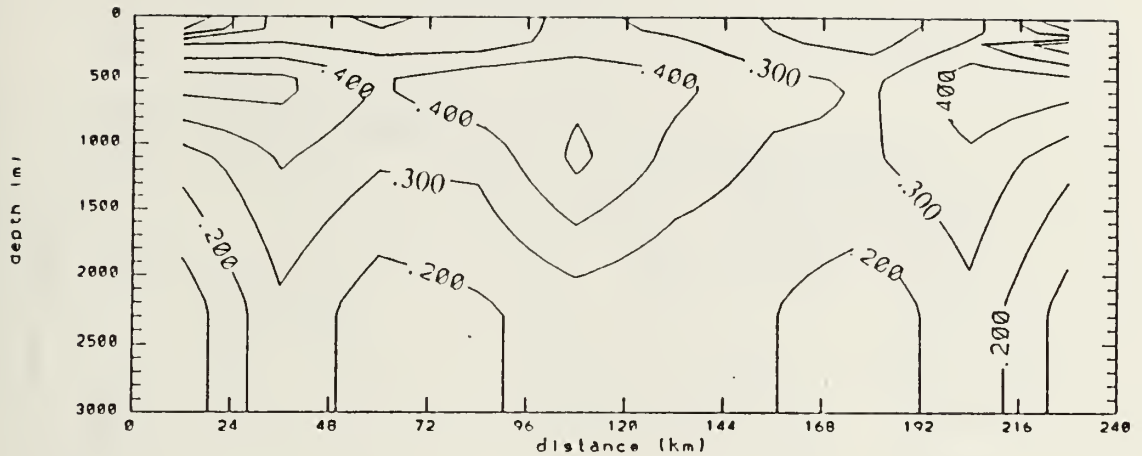


Figure 10. Resolution Kernel Peak Values Using Depth Dependent Variability: A value of 1.0 implies a box is well resolved.

In our modeling of the Greenland Sea, we assume the variability of sound speed perturbations and currents decrease exponentially with depth, though each variable may be parameterized by a different folding depth. Reasonable surface RMS δc values may be estimated from sea surface temperature measurements derived from satellite data and ship observations. Surface current variability may be estimated from drifting buoy and CTD stations at the array moorings. Since surface values may be more reliably determined, the focus of our sensitivity study is placed on the effect of uncertainty in subsurface variability. The computer simulated ocean on which inversions were performed had a surface RMS δc of 6 m/s and a folding depth equal to 1000 m. The estimator is provided with the same surface value and then we compare model performance using folding depths of 500 m, 1000 m, and 3000 m. A similar sensitivity study is conducted in current tomography. The surface RMS current for the computer generated ocean and the estimator is 10 cm/s. The ocean was generated using a folding depth of 700 m. System performance is evaluated using folding depths 350 m, 700 m, and 2100 m in the estimator. Figure 12 shows the depth dependent variability curves at different folding depths. The estimator and the simulated ocean both use an average value based on these curves for each layer of the discretized ocean.

A longer folding depth used in the estimator implies the system expects greater variability in the unknown field at depth. We define the half-depth, $\%Z_{.5}$, as the percent

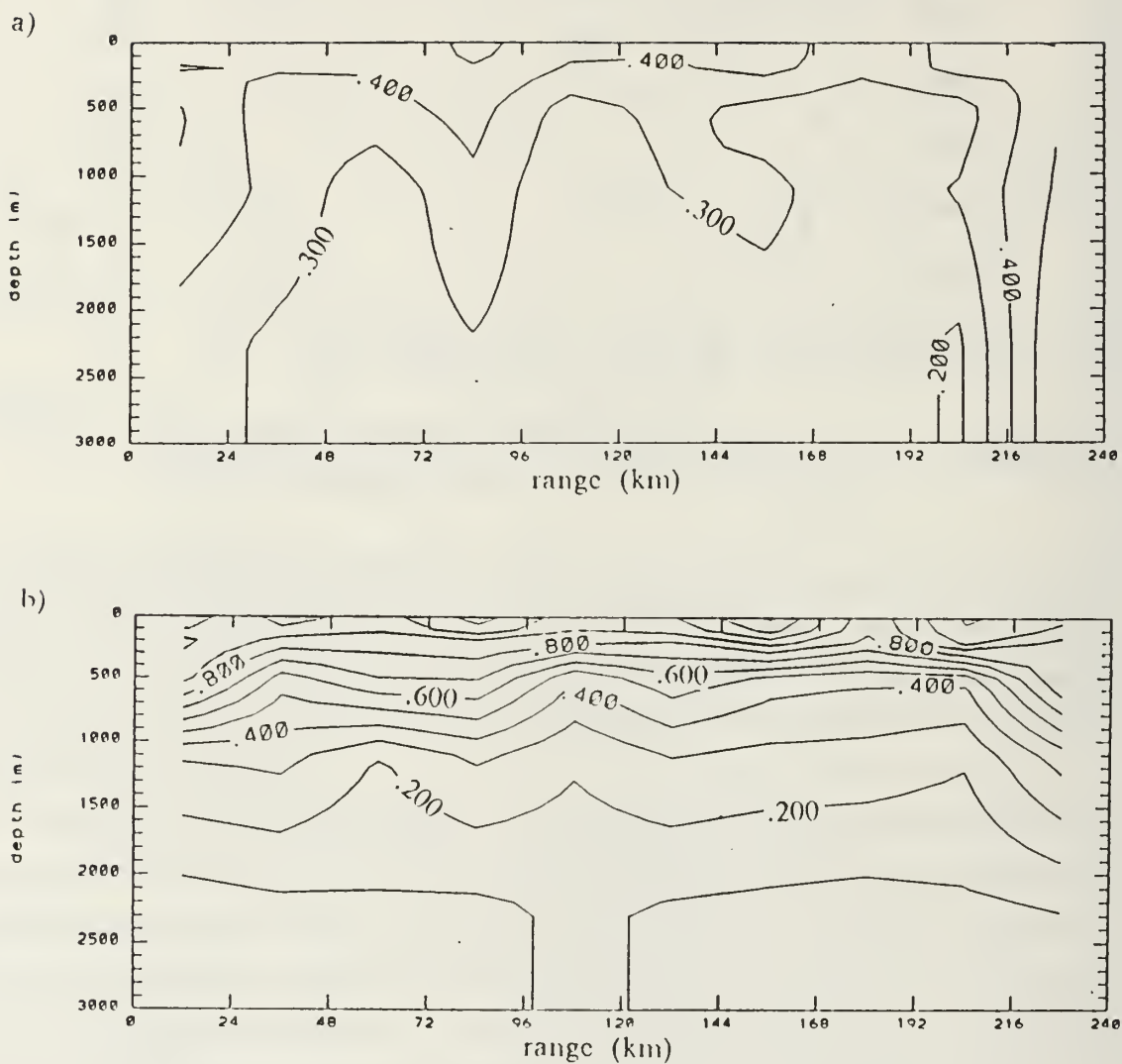


Figure 11. Standard Deviation of the Estimate (m/s): a) RMS δc is constant throughout ocean volume. b) RMS δc is exponentially decreasing with depth.

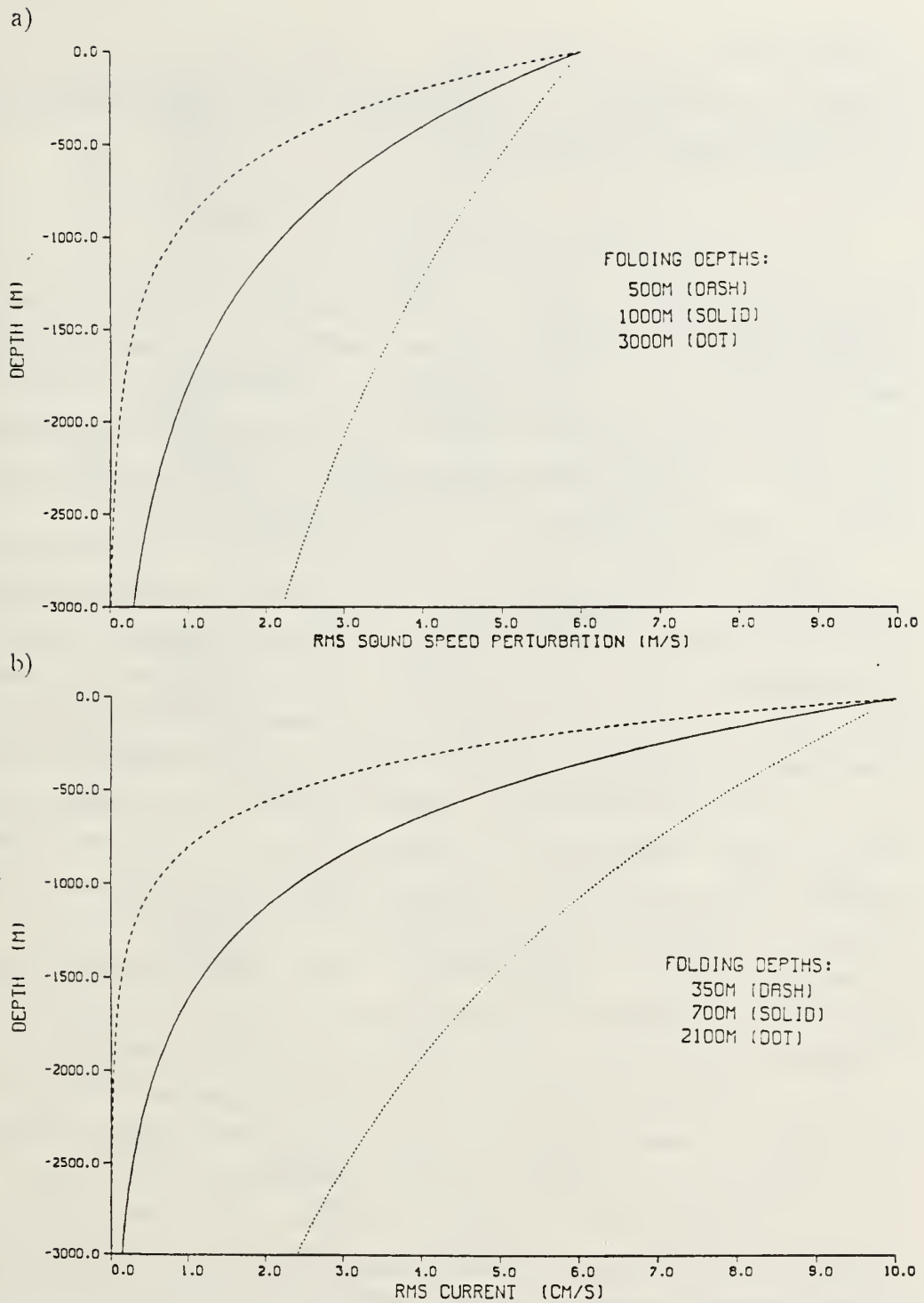


Figure 12. Depth Dependent Variability Curves at Various Folding Depths: a) Density tomography curves. b) Current tomography curves.

of the ocean measured from the surface which contains 50% of the integrated variability over the ocean depth. It is expressed as

$$\%Z_s = \frac{f}{z_{ocn}} \left[\ln(0.5 + 0.5e^{\frac{z_{ocn}}{f}}) \right] 100\% \quad (3.4)$$

where f is the folding depth and $z_{ocn} = -3000$ m, is the bottom depth. Note that we have defined f so that it is positive in our application here, that is $f > 0$ implies variability with depth decreases. However, z_{ocn} is negative to be consistent with our upward pointing positive z -axis with $z = 0$ m at the surface. It is interesting to note that the half-depth depends only on the folding depth and ocean depth, but not on the surface value. This allows us to make comparisons between the two areas of tomography.

In Figure 13a, we show the top three layers of a simulated sound speed perturbation field using the VTL approach. Figures 13b, 13c, and 13d show the corresponding estimated fields based on folding depths of 500 m, 1000 m, and 3000 m, respectively. The simulated field has $\%Z_s = 21.5\%$, or half of the integrated variability is contained in approximately the top fifth of the ocean. An estimator using a folding depth at 500 m expects half of the integrated variability to be contained in roughly the top 10% of the ocean. As the acoustic signal passes through lower regions of the ocean, the signal encounters higher variability than the estimator expects. The estimator interprets this “energetic” data as the result of more intense structures in the upper ocean than are truly present. The solution is constructed accordingly. The opposite effect occurs when the assumed folding depth is larger than the true value. With $f = 3000$ m, the estimator assumes the ocean contains half the variability in the top 40% of the ocean and tends to smooth the variability over greater depths than found in the true solution.

We have made the assumption that variability is an exponential distribution. Under these conditions, the estimator is more sensitive to underestimating the folding depth than overestimating it. Figure 14 shows the relationship between f and $\%Z_s$. The slope of the curve indicates system sensitivity. For a given folding depth, the slope is greater when the assumed value is less than the true folding depth, indicating the system’s increased sensitivity to underestimation. Since the sensitivity measured by $\%Z_s$ is dependent only on folding depth and ocean depth, we can also see from Figure 14 that when true folding depths are small, the system is more sensitive to both underestimation and overestimation than when the true folding depth is large.

For current tomography, we find a similar trend. Figure 15a shows a simulated current field in the top three layers of the ocean. Figures 15b, 15c, and 15d show the

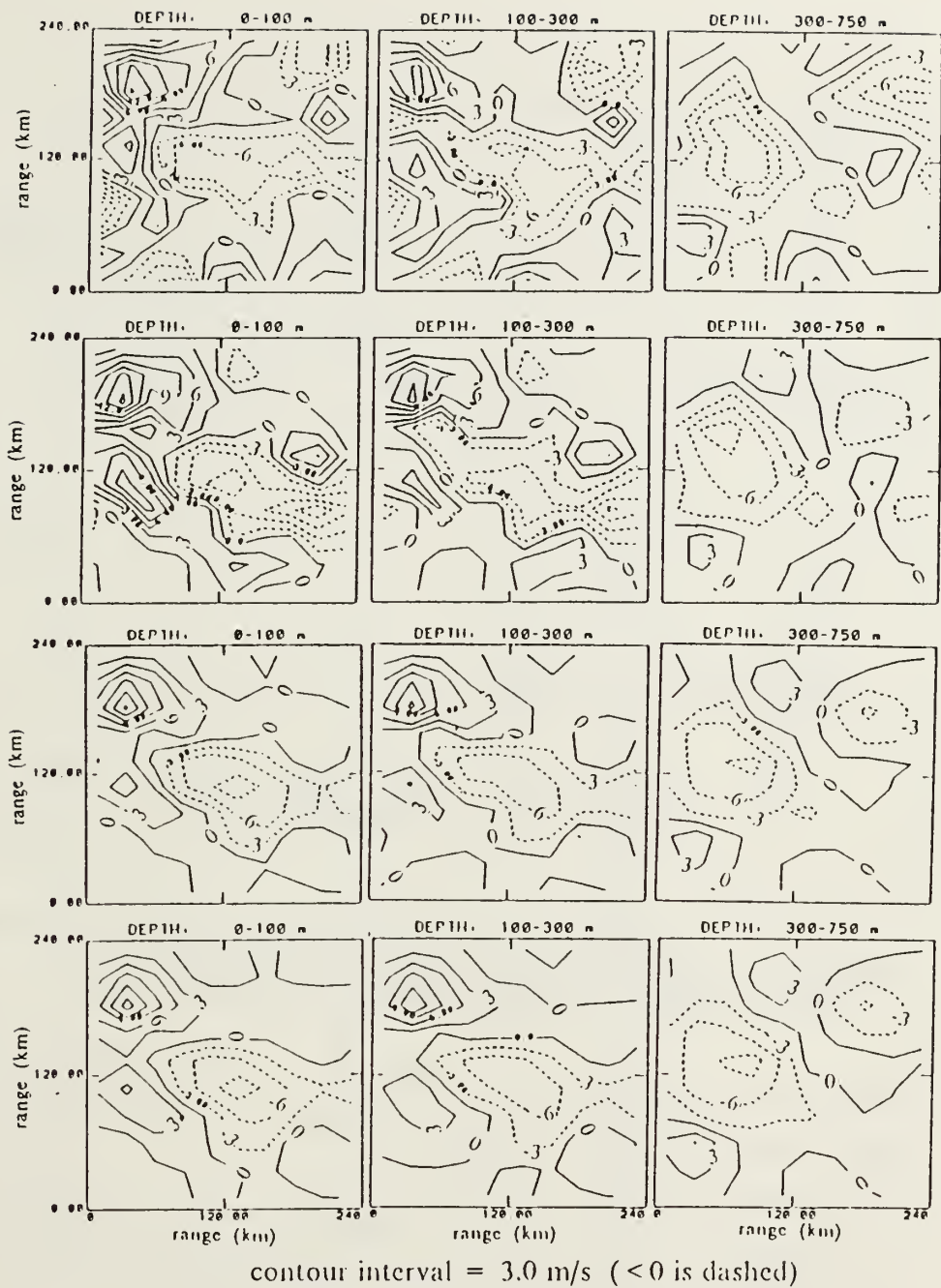


Figure 13. Perturbation Estimator Response Using Various Folding Depths: a) Simulated δc (m/s), $f = 1000$ m. b) Estimated δc (m/s), $f = 500$ m. c) Estimated δc (m/s), $f = 1000$ m. d) Estimated δc (m/s), $f = 3000$ m.

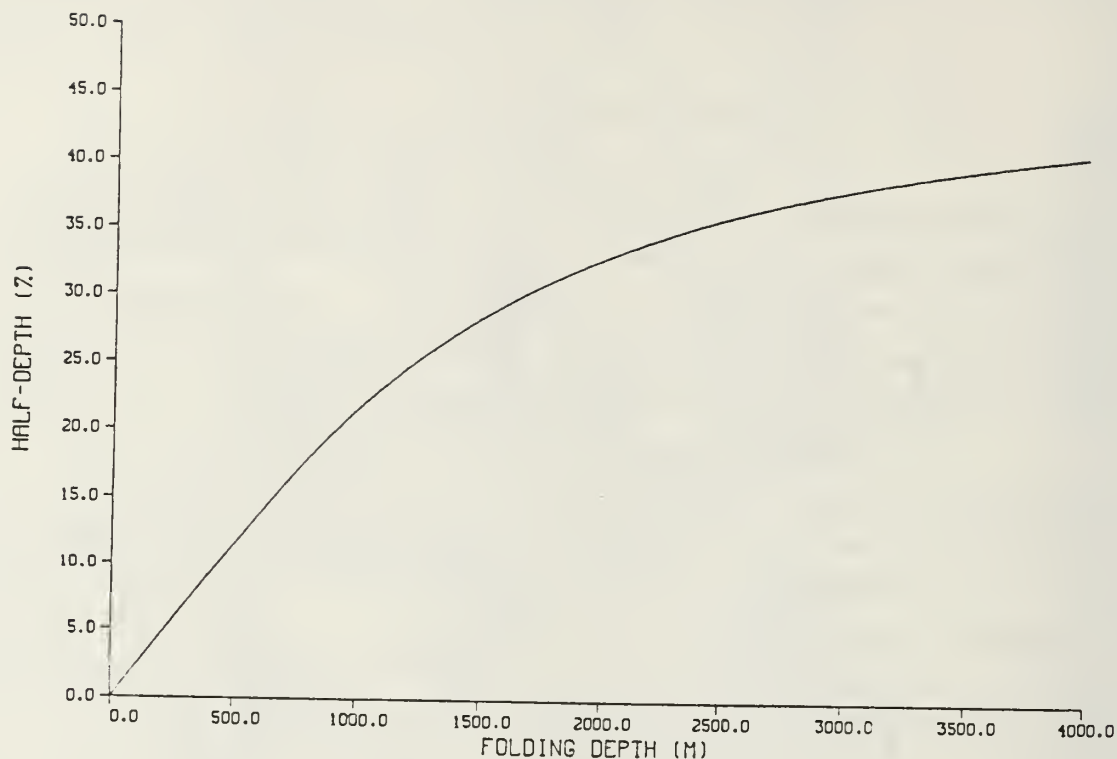


Figure 14. Half-depth as a Function of Folding Depth: Slope indicates model sensitivity to estimating true folding depth.

corresponding estimates based on folding depths of 350 m, 700 m, and 2100 m, respectively. As in our density tomography, the estimator is more sensitive to underestimating the folding depth than overestimating.

These results of these sensitivity studies are based on the assumption that the true variability distribution is an exponentially decreasing function with depth. If the distribution is significantly different from this, our results may not apply, however, the variation of the half-depth as a function of some other applicable parameter may still be a useful measure of sensitivity.

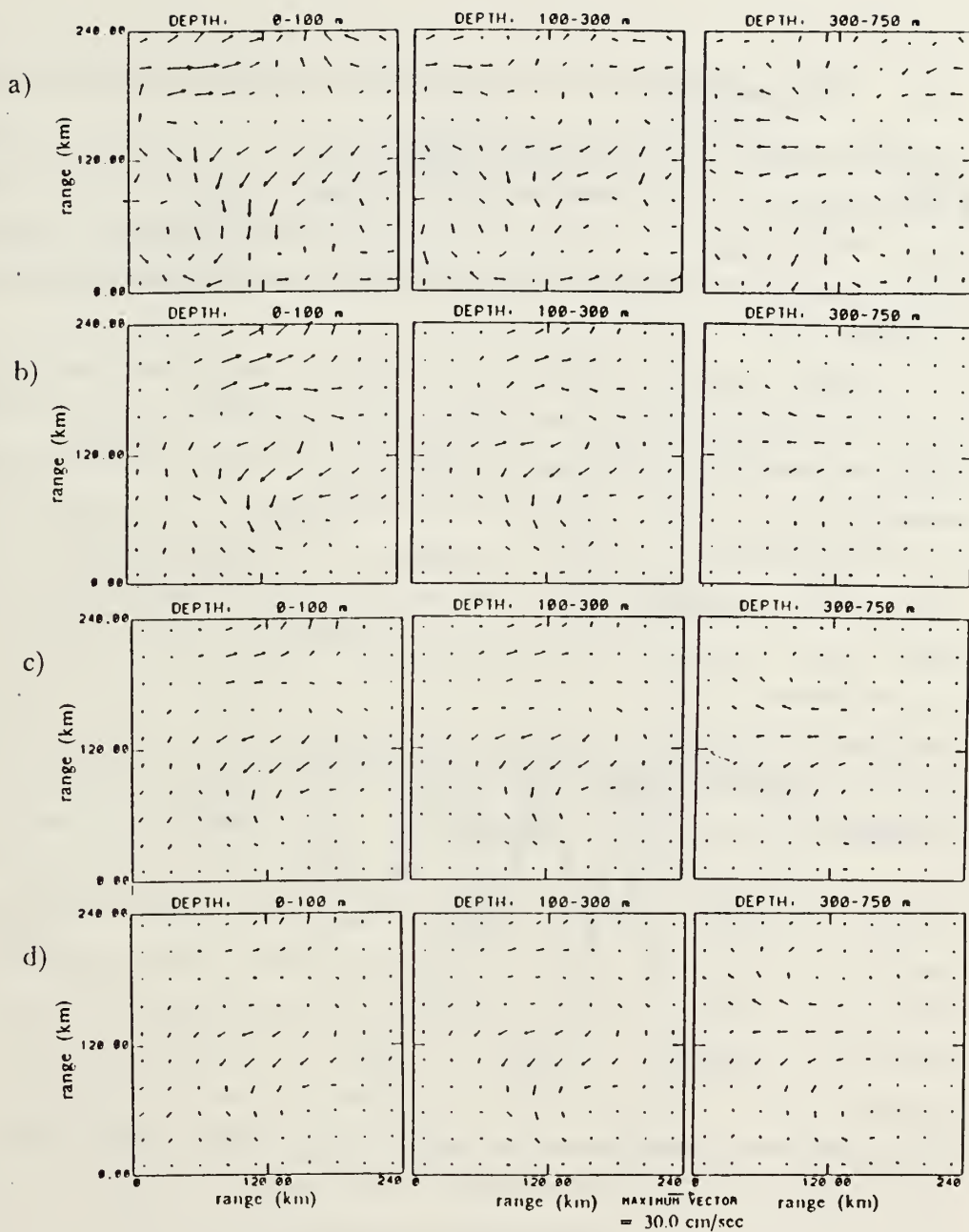


Figure 15. Current Estimator Response Using Various Folding Depths: a) Simulated currents, $f = 700$ m. b) Estimated currents, $f = 350$ m. c) Estimated currents, $f = 700$ m. d) Estimated currents, $f = 2100$ m.

IV. PRELIMINARY INVERSIONS USING GREENLAND SEA DATA

The discussions from the previous chapters have given us insight into the expected system performance in the Greenland Sea environment. However, the use of simulated oceans cannot explore every aspect of system performance. Only using actual data from the tomographic array can disclose the extent of success the system will have as an ocean monitoring tool.

At present, a set of travel time measurements from transmissions between Mooring 4 and Mooring 5 has been processed for our analysis by WHOI. Acoustic signals were transmitted six times a day on every third day starting in late September, 1988, and ending in late July, 1989, covering the winter cooling season. The complete set of data for transmissions from Mooring 4 to Mooring 5 is used in our preliminary study. The quality control "goodness estimates" of some data are, however, less than optimal. In future studies, a criterion for the minimum acceptable goodness estimate may be set. For our preliminary study, we use for each ray an average of all six transmissions to determine the travel time of the day. The data indicate three bundles of eigenrays were resolved from signal processing at WHOI. We will make reference to each bundle by the magnitude of its nominal receiving angle. The bundles consist of four rays at 13° , four rays at 10° , and one ray at 0° . Using a sound speed profile based on CTD taken near the center mooring, our ray tracing algorithm predicts four eigenray paths near 13° and four paths near 9° which we use for our data inversion. Since the algorithm fails at shallow angles, the 0° ray path is constructed by an alternate method. We trace an axial path along the minimum sound speed axis, which is located approximately 30 m above the source depth. The sound speeds at the source and receiver depths are less than .3 m/s greater than the minimum sound speed of the reference profile. We feel this is a good approximation for the 0° ray since WHOI identified this arrival by using the last signal peak which was very much bigger than noise (Pawlowicz, 1991). To display our results, we have taken a vertical slice in y-range as shown in figure 16a. This slice contains Mooring 4 and Mooring 5. The selected eigenray paths, projected onto the vertical slice, are shown in figure 16b.

To evaluate system performance and analyse the data, we divide the ocean volume into 500 boxes using the VTL layering scheme described in Chapter III. Using this scheme, the source at Mooring 4 is in the top ocean layer where $48\text{km} \leq x \leq 72\text{km}$, while

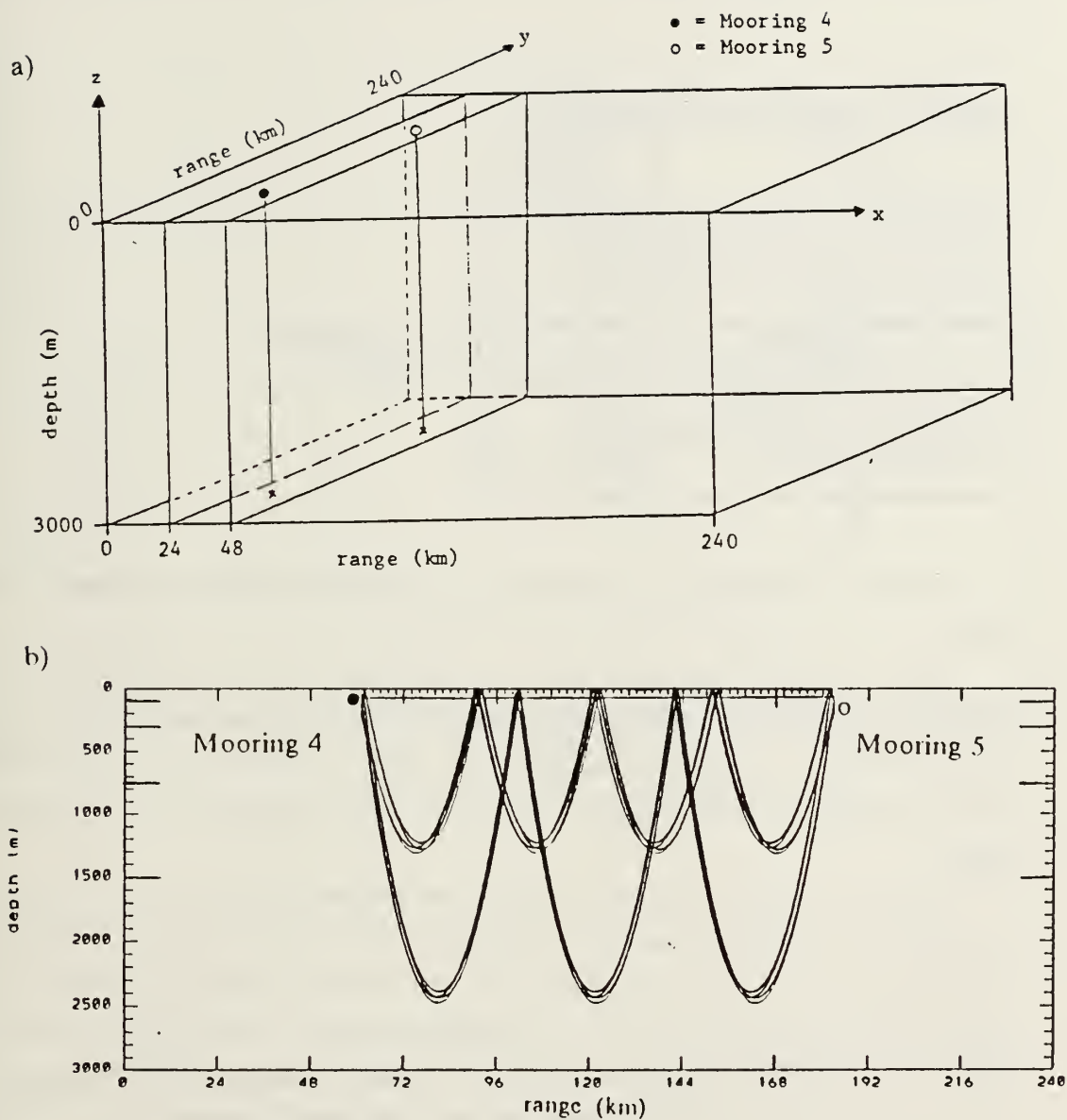


Figure 16. Vertical Slice and Eigenray Paths for Moorings 4 and 5: a) Orientation of vertical slice used to display model output and system performance in the vicinity of Moorings 4 and 5. b) Selected eigenrays projected onto the vertical slice.

the receiver at Mooring 5 is in the second layer from the top where $168\text{km} \leq x \leq 192\text{km}$. We set the *a priori* knowledge for the estimator as shown in Table 3.

Table 3. SYSTEM PARAMETERS

Parameter	Assumed Value
Surface RMS δc	6 m s
Folding Depth	1000 m
Random Noise	1 ms
Correlation Length (x,y)	30 km
Correlation Length (z)	300 m

Once the system parameters are established, the estimator's performance may be evaluated.

Figure 17 displays the resolution kernel peak values. The resolution of the system is highest in the vicinity of the moorings since this is where the three sets of rays converge. The higher resolution in the upper 1000 meters is due to the exponential distribution of variability and path length contributions from both the 10° and 13° rays in this region.

Another measure of system resolution is the minimum resolution length. As shown in figure 18, the minimum resolution length in the y direction is about 60 km near the top center portion of the vertical slice and near the source and receiver sites, and increases rapidly where there are few or no eigenray paths. The relatively low values are due to the convergence of all three ray groups in these regions. Ocean features smaller than the minimum resolution length are not adequately resolved and will appear smoothed in the estimate. That is, we expect the estimator to generate less intense and more spread out features than the true structure if the true solution has a length scale less than the resolution length at its location. Since we are using a two point system which has a north-south (y-direction) orientation, there is virtually no resolution of features in the x-direction. As more data become available from other moorings, the estimator will gain more information in all dimensions. Figure 19 shows the vertical minimum resolution length which also tends to be lowest where the three groups of rays

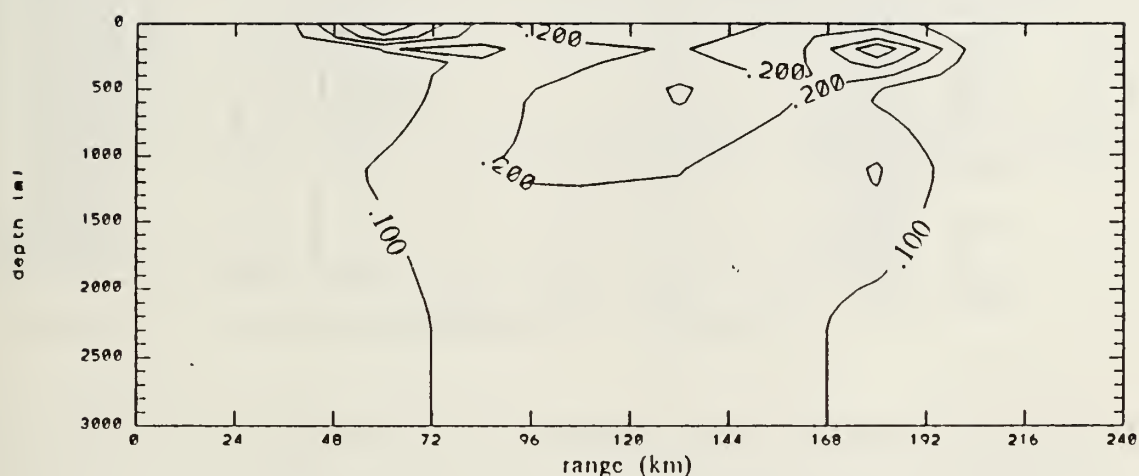


Figure 17. Resolution Kernel Peak Values for Greenland Sea Data Inversion: A value of 1.0 implies a box is well resolved.

converge. However, it is interesting to note the unusually large minimum resolution length of 1700 m in the top center of the slice. It appears to be an anomalous feature caused by the arbitrary choice of the the coordinate system. The exact cause of this locally high value, however, needs further investigation.

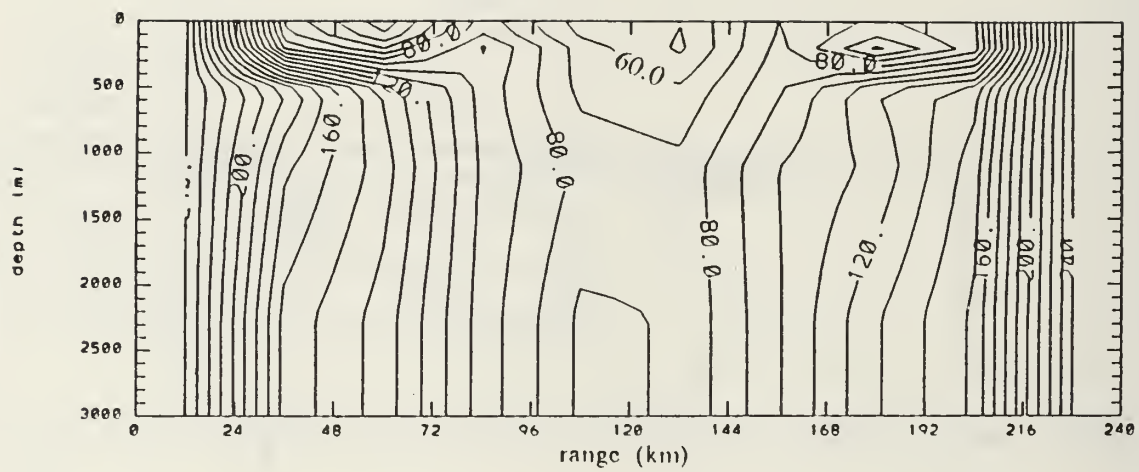


Figure 18. Y-Direction Minimum Resolution Length (km)

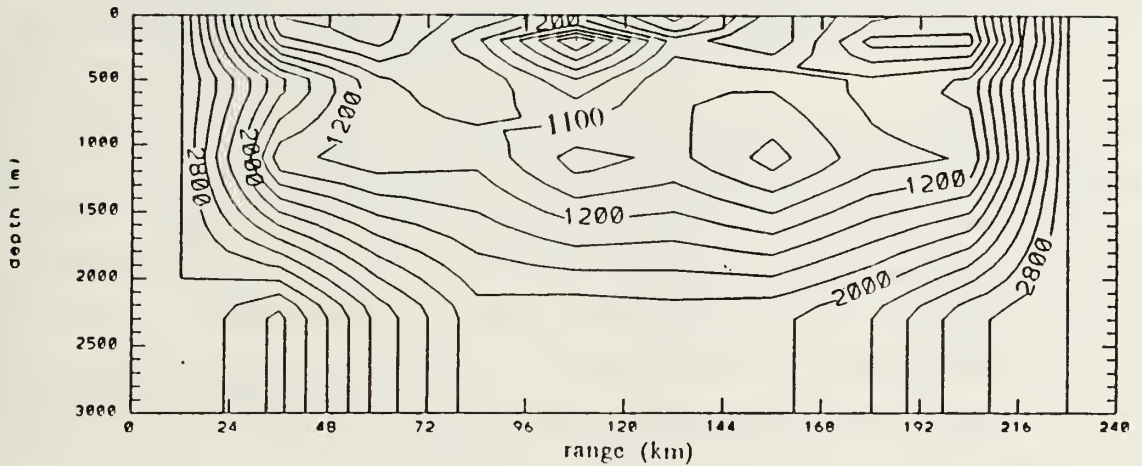


Figure 19. Z-Direction Minimum Resolution Length (m)

The fact that the system has low resolving power is not surprising since there are only three bundles of eigenrays involved. By using depth dependent variability in the estimator, we have concentrated the resolution of the system in the upper ocean. Since $\text{RMS } \delta c$ varies with depth, we normalize the RMS error to show that the system minimizes error in the upper ocean, the region of interest. Figure 20 depicts the RMS error as a percent of the assumed variability in the layer.

Producing sound speed perturbation estimates with our estimator requires we convert the travel time measurements from the array to travel time perturbations with respect to a reference ocean. Once the sound speed perturbations have been estimated, we can use Equation (2.6) to determine an estimated sound speed field of the Greenland Sea.

For each of the nine eigenrays identified by WHOI, a time averaged value was calculated. The corresponding travel time differences between the nine time averaged Greenland Sea values and the nine predicted eigenray arrivals based on ray theory range from 200-300 milliseconds. The differences are largely due to structural differences between the model ocean used to predict our ray paths and the "time averaged" Greenland

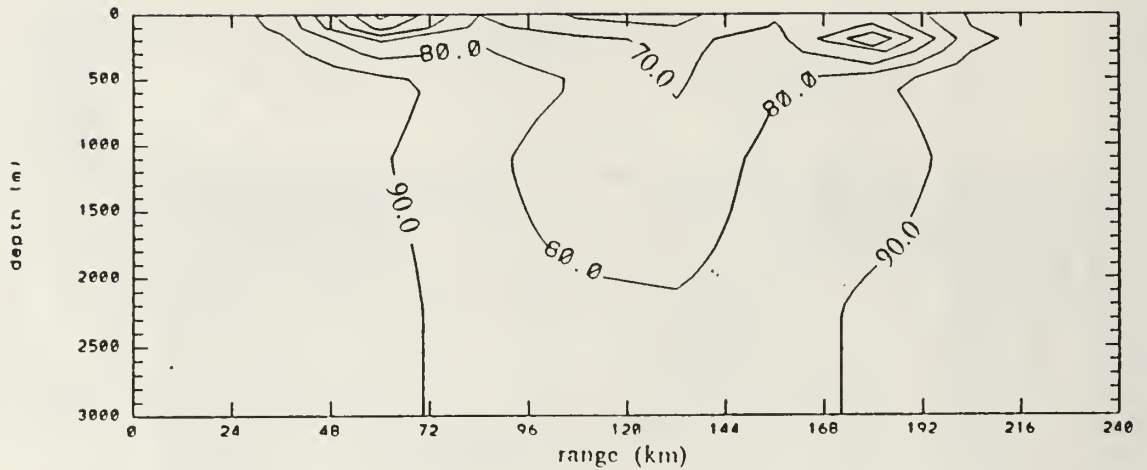


Figure 20. Percent RMS Error

Sea, however, model errors in mooring positioning and in travel time calculations from our ray theory based algorithm may also contribute significantly to the differences. Based on receiving angles and sound speed data taken at the mooring sites, we have a high degree of confidence in the positioning of the ray paths within the discretized boxes. Even in a worst case scenario, the 200-300 millisecond differences would imply less than 500 meter differences in corresponding path lengths over total path lengths in excess of 120 km. These differences will not affect the linear operator of the estimator greatly.

Errors in travel time calculations even as low as tens of milliseconds, however, may contribute significant errors in the estimates since they are treated by the estimator as part of the data. The scale of δT in the Greenland Sea is on the order of tens of milliseconds, based on differences between daily travel times and the averaged travel time of each of the rays. Though we cannot eliminate these errors, we can separate the errors from our time series of estimates by basing the travel time perturbations on the time averaged ocean. By choosing the time averaged ocean as our reference state, we can observe the response of the estimator over the winter cooling season without superimposing the effects of model travel time errors. The structure of the time averaged ocean

is not known, however, and may have range dependent features of interest. We can find this structure with respect to the known sound speed structure used to predict our ray paths by inverting the travel time differences between corresponding rays of the model ocean and the time averaged data from the real ocean. From this information, we can find the sound speed structure of the Greenland Sea.

Figure 21 shows the estimated δc field of the time averaged ocean referenced to the ocean used to predict our ray paths. To produce this field, we increased the horizontal correlation lengths of the estimator to 100 km based on the expectation that the time averaged ocean is more highly correlated than any of the daily perturbation fields we estimate. The solution shows a reasonable trend. The time averaged ocean is expected to be cooler in the upper ocean since the ocean used for ray prediction is based on a profile taken in September, a relatively warm time in our data collection period. However, the accuracy of the predicted structure is affected by travel time errors from the ray tracing algorithm and mooring positioning in the model. An independent source of data is needed to verify the extent of the effects, but positioning errors may be reduced as more data sets of the array are included.

Once the system produces the first estimated perturbation field, there is little increase in computational effort to generate a time series of solutions using the same estimator. To demonstrate the response of the estimator using the Greenland Sea data from WHOI, we plot a time series of the average δc based on the top two model layers at the position of Mooring 4 and Mooring 5. The time series are shown in Figures 22a and 23a respectively. The general "spikiness" of the plots is the result of having a two point system which bases solutions on only three groups of eigenrays. It is difficult for the estimator to precisely position features with so little information. The features appear to move more abruptly in sequential solutions than could be physically be expected, indicating instability of the solutions. The inclusion of data from other moorings will increase the estimator's knowledge of the structures in the vicinity of Moorings 4 and 5, and the solutions are expected to show greater stability over time. However, even with instability affecting the short term solution, there are indications of trends at longer time scales detected. The seasonal cooling and warming through the fall, winter, spring and early summer time frame are evident at both moorings. Since sound speed is directly related to temperature (Mackenzie, 1981), δc decreases with winter cooling and increases with spring and summer warming. Events at the 20-90 day scale are extracted from the time series by applying a time domain filter with cutoff frequency .05 cycles day at each

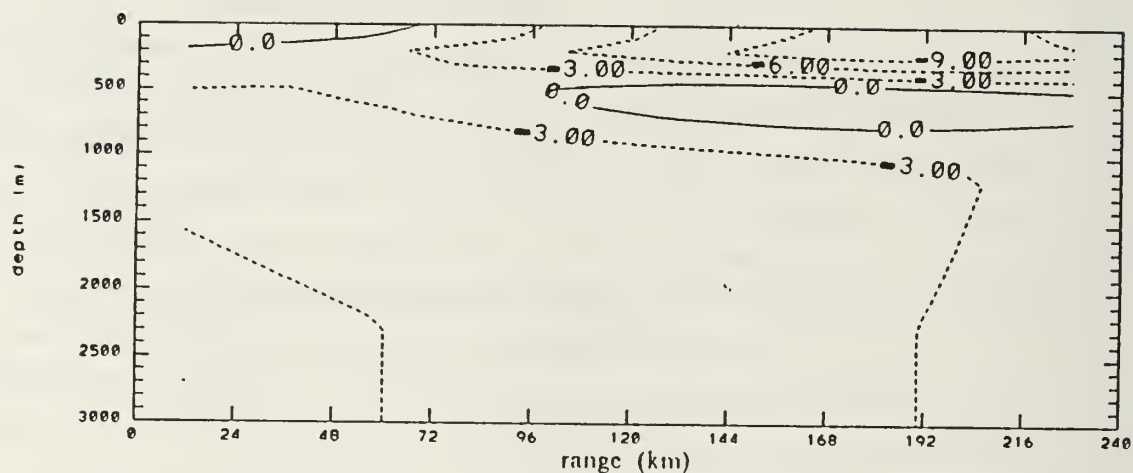


Figure 21. Sound Speed Perturbations of the Time Averaged Ocean (m/s): The sound speed structure of the time averaged ocean is the sum of this field and the sound speed structure of the ocean used to predicted eigenray paths.

of the point estimates. The time series of the filtered solutions near Moorings 4 and 5 are shown below their respective unfiltered versions in Figures 22b and 23b.

Environmental temperature data taken at Moorings 4 and 5 sites at a depth of 100 meters has been provided by WHOI and are displayed in Figures 22c and 23c. Comparing the filtered δc estimates to the respective temperature data provides evidence that the two point tomographic system is detecting synoptic scale events. Mooring 5 particularly shows good correlation between temperature and the local δc estimates. Of spe-

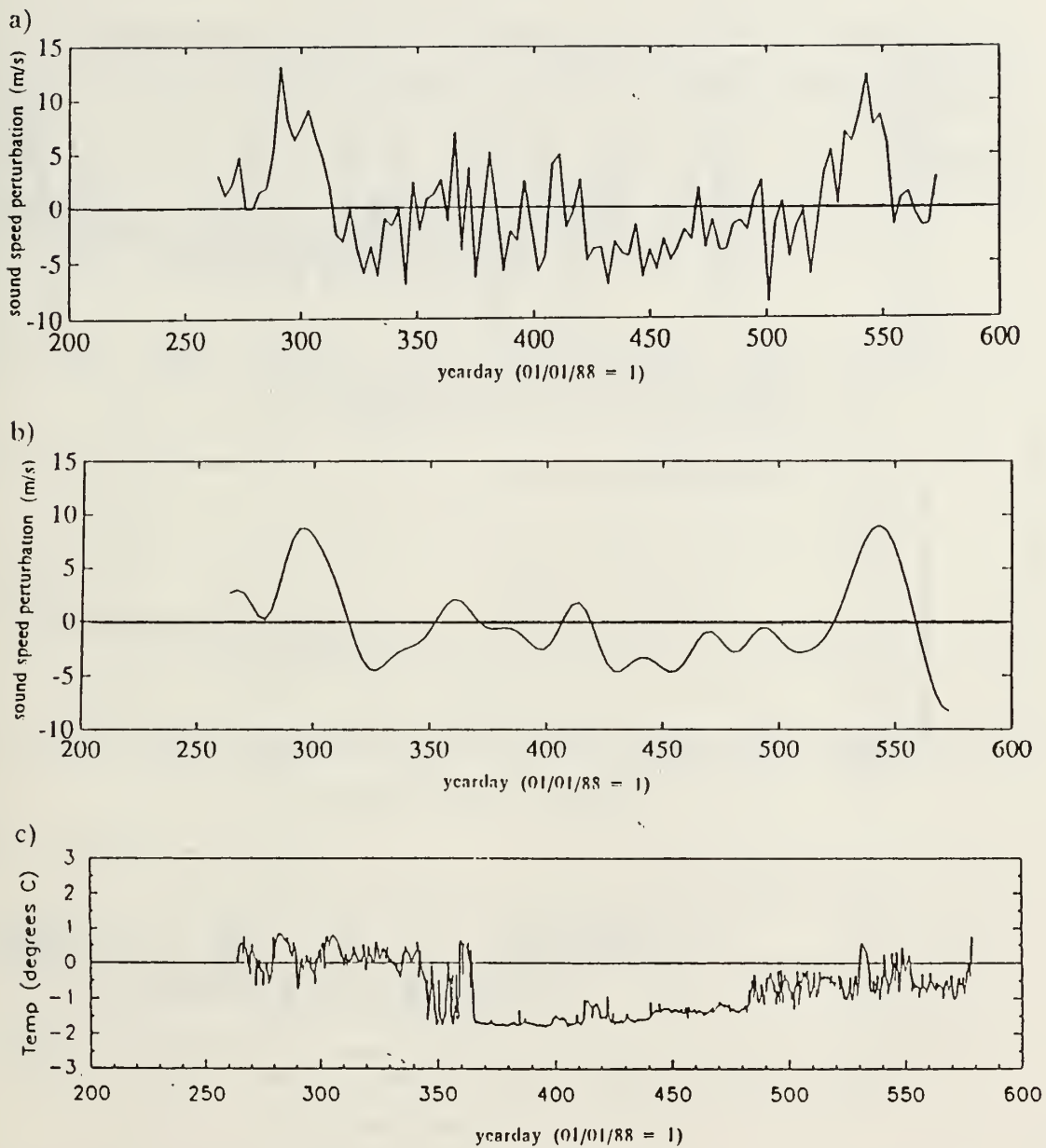


Figure 22. Sound Speed Estimates and Temperature Data Near Mooring 4: a) Unfiltered time series of estimates. b) Filtered time series of estimates using cutoff frequency = .05 cycles/day. c) Temperature data provided by WHOI.

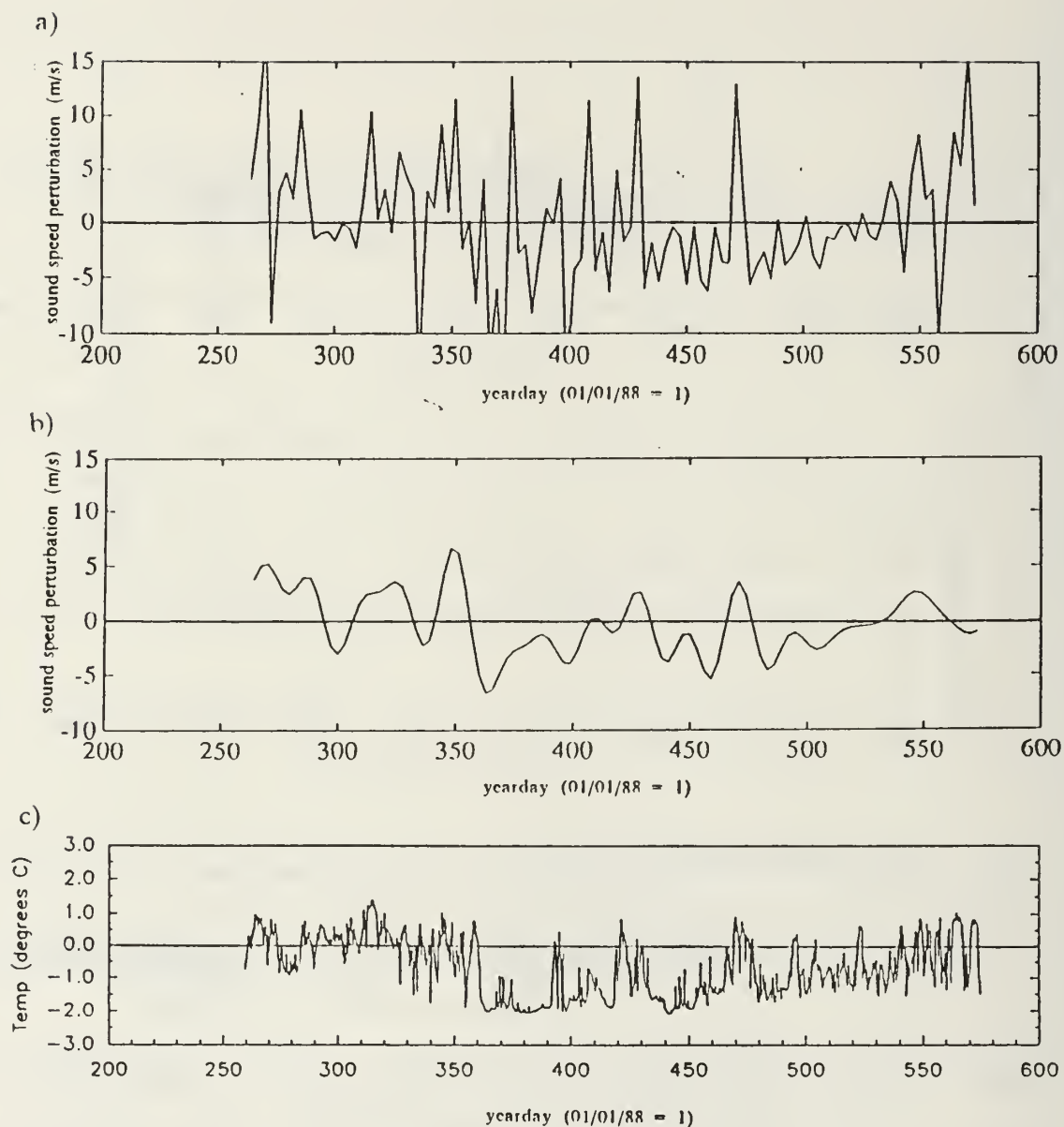


Figure 23. Sound Speed Estimates and Temperature Data Near Mooring 5: a) Unfiltered time series of estimates. b) Filtered time series of estimates using cutoff frequency = .05 cycles/day. c) Temperature data provided by WHOI.

cific interest are the detection at Mooring 5 of the strong cooling event near yearday 360 and the corresponding responses to warming and cooling from yearday 390 to about yearday 560.

As an example of system output, a sequence of seven δc fields covering a three week period from yeardays 462 to 480 at three day intervals is displayed in Figures 24-30. The temperature record at Mooring 5 indicated that a strong warming event followed by a strong cooling event occurred during this period while a weaker pair of warming and cooling events occurred near Mooring 4. The output of the estimator is consistent with the temperature data and reflects these trends.

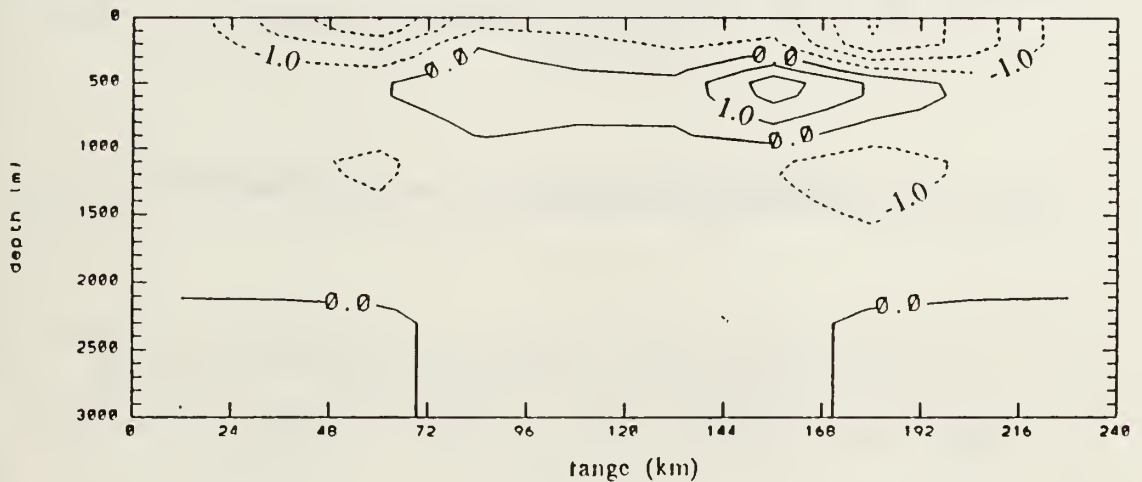


Figure 24. Sound Speed Perturbation Estimates (m/s), Yearday 462

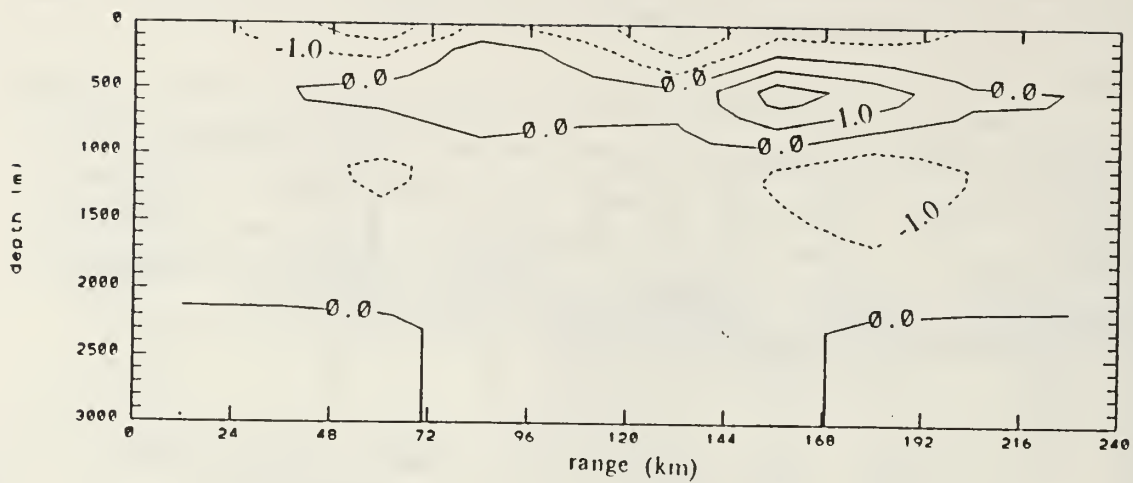


Figure 25. Sound Speed Perturbation Estimates (m/s), Yearday 465

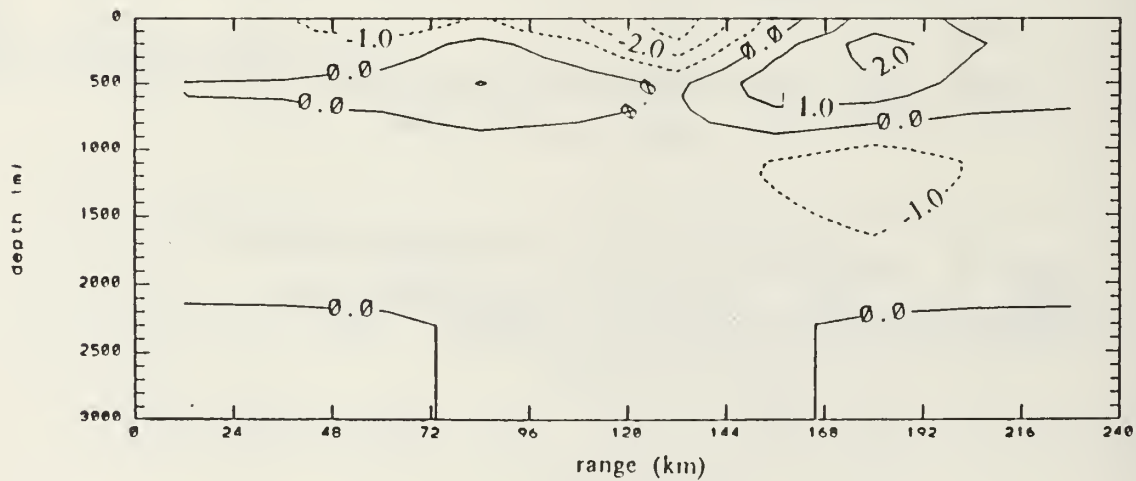


Figure 26. Sound Speed Perturbation Estimates (m/s), Yearday 468

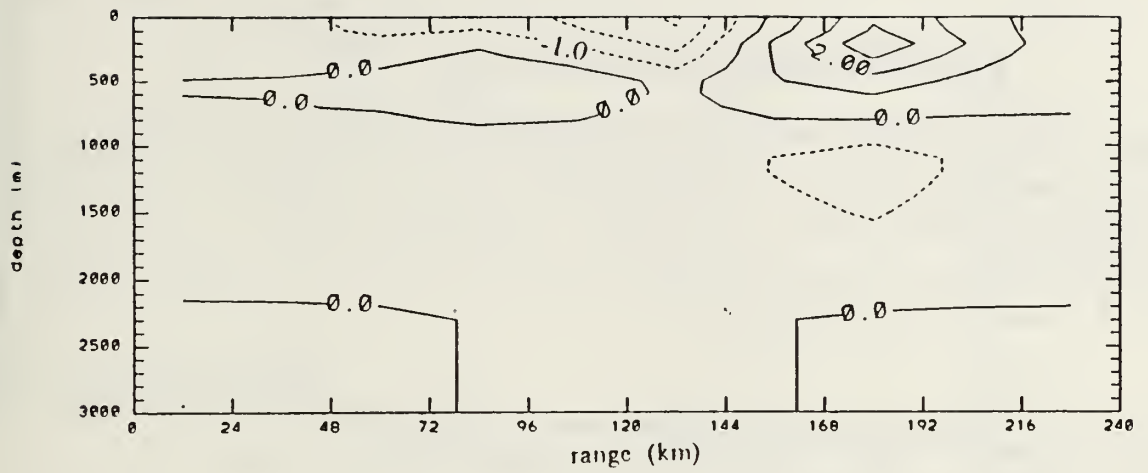


Figure 27. Sound Speed Perturbation Estimates (m/s), Yearday 471

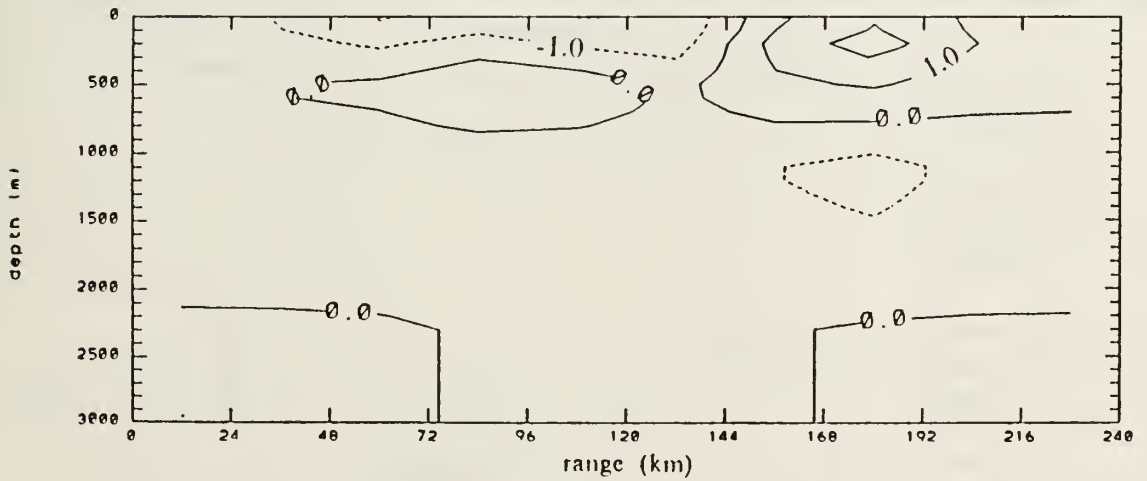


Figure 28. Sound Speed Perturbation Estimates (m/s), Yearday 474

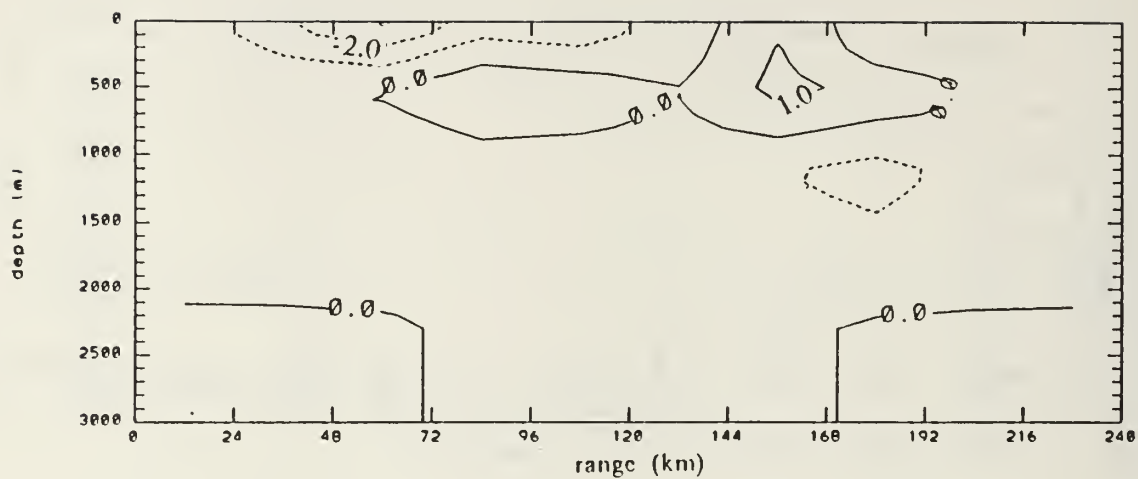


Figure 29. Sound Speed Perturbation Estimates (m/s), Yearday 477

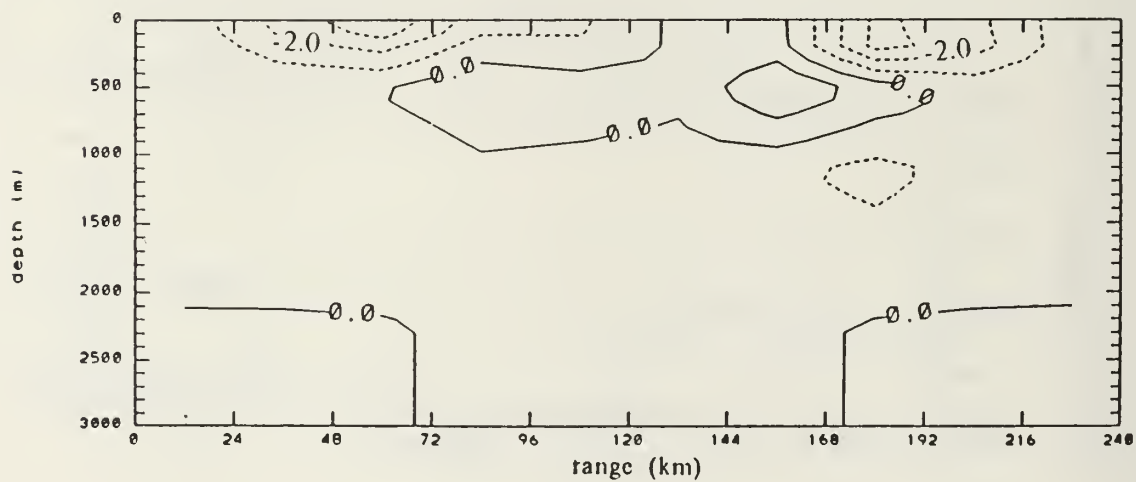


Figure 30. Sound Speed Perturbation Estimates (m/s), Yearday 480

V. CONCLUSIONS AND RECOMMENDATIONS

In this thesis, we discussed the advantages and problems of using a ray theory based algorithm to establish the forward problem, developed an inversion code which could be applied to Greenland Sea data, and tested this code using available Greenland Sea data. Here we offer some conclusions and recommendations for further study in this area.

A. CONCLUSIONS

First, we looked at the advantages and problems associated with using an algorithm based on ray theory to model eigenray paths for the Greenland Sea tomography array. Ray theory provides a simple depiction of eigenrays paths and the algorithm is coded with uncomplicated mathematics. However, CTD data from this area shows an acoustically difficult environment may exist at least during part of the year and degrade the reliability of the predicted eigenray paths. Strong gradients and rapidly changing gradients in the vicinity of the transceiver elements can strongly affect model output. Rays which are predicted to be turned in the gradient or near the sharp change in gradient are strongly influenced by small changes in the sound speed profile in this region. These significant differences reduce the reliability of the resulting ray path. The algorithm often fails when predicting paths for rays launched at shallow angles. Rays launched at steeper angles pass through these regions at greater angles and are less affected. These ray paths are more reliable.

Data prepared by WHOI indicates resolvable eigenrays between Mooring 4 and Mooring 5 are at large enough launch angles that they are not turned in the sharp gradient. Thus, our algorithm is adequate to model the forward problem in this environment.

In our inversion code development, we investigated the effects of using variable thickness layers vice an equally spaced scheme to discretize the Greenland Sea for the estimator. Using thinner layers in the upper ocean and thicker layers in the lower ocean, we kept the total number of boxes the same. The advantages of using this scheme is that it provides more solution detail in the region of interest for the same computational effort. However, since the thick lower layers contain greater path length in this layering scheme, system resolution shifts toward the lower ocean. However, by specifying a depth dependent variability in the covariance of the unknown field, we tell the estimator

to expect greater variability in the upper ocean. As a result of this modification, system resolution shifts back towards the upper ocean. For our purposes, we have modeled the depth dependent variability as an exponentially decreasing function with depth. If more accurate information is known, it could just as easily be used.

Since the true variability may not be known, we investigated model sensitivity to uncertainty in variability distribution. Using an exponentially shaped variability distribution as our basis, we looked at the effects of underestimating and overestimating the characteristic folding depth of the distribution. Defining the half-depth as the percent of the ocean measured from the surface which contains 50% of the integrated variability, we have an objective means of measuring sensitivity. The half-depth gives us an idea of how the estimator is distributing variability in the ocean. We have shown the change in half-depth per unit change in folding depth is always greater when the true folding depth is underestimated. We have also shown from the same relationship that at smaller true folding depths, the model is more sensitive to both underestimation and over estimation. Half-depths relationships can be developed for other variability distributions and applied in similar ways to measure model sensitivity.

Our inversion method was tested by using available data from the Greenland Sea array as input to our model. The system used nine eigenray paths between the source at Mooring 4 and the receiver at Mooring 5. The results of our preliminary application of the model show evidence of detection of the seasonal cooling cycle and detection of synoptic scale events at time scales of 20-90 days. The two point system also shows unrealistically large fluctuations in the solutions at periods of less than 20 days. This indicates instability of the solutions, however, we expect stability to increase as more data becomes available from other moorings.

Our acoustic tomography code is ready for application to Greenland Sea data. The estimator can provide concentrated estimates in the region of interest and allows for a depth dependent variability distribution of the unknown variable. With these modifications, our model can use tomographic data to monitor changes in ocean structure.

B. RECOMMENDATIONS

CTD data has shown that the near surface structure of the Greenland Sea is challenging to model acoustically. Though our ray theory based algorithm seems adequate for our purposes here, the combination of the near surface gradients and transceiver location make this algorithm less than ideal. However, the convenience of using a ray theory based algorithm to model the lower ocean stills keeps it an attractive basis for

sound propagation prediction. We recommend that a more accurate means of establishing the forward problem in the Greenland Sea be investigated, perhaps using a hybrid of ray theory and normal modes.

Based on the promising results using just a two point system, continued analysis of the Greenland Sea using this code and data from the remaining 14 mooring paths of the deployed array should yield useful estimates of ocean circulation and be able to detect large scale convective events.

REFERENCES

- Backus, G. E. and J. F. Gilbert, "Numerical Applications of a Formalism for Geophysical Inverse Problems", *Geophysical J. R. Astron. Soc.*, 13, 247-276, 1967.
- Chiu, C. S. and Y. Desaubies, "A Planetary Wave Analysis Using the Acoustic and Coventional Arrays in the 1981 Ocean Tomography Experiment", *Journal of Physical Oceanography*, 17, 1270-1287, 1987.
- Chiu, C. S., J. F. Lynch, and O. M. Johannessen, "Tomographic Resolution of Mesoscale Eddies in the MIZ - A Preliminary Study", *Journal of Geophysical Research*, 92(C7), 6886-6902, 1987.
- Cornuelle, B. D., and Collaborators, "Tomographic Maps of the Ocean Mesoscale. Part 1: Pure Acoustics", *Journal of Physical Oceanography*, 15, 133-152, 1985.
- DeFerrari, H. A. and H. B. Nguyen, "Acoustic Reciprocal Transmission Experiment, Florida Straits", *The Journal of the Acoustical Society of America*, 79, 299-316, 1986.
- Gerald, C. F., *Applied Numerical Analysis*, 4th ed., Addison Wesley, Inc., 1989.
- Greenland Sea Sience Planning Group, *Greenland Sea Project - An International Plan of the Arctic Ocean Sciences Board*, 1986.
- Kao, C. C., *A Study of the Sensitivity of the Greenland Sea Acoustic Tomography*, Master's Thesis, Naval Postgraduate School, Monterey, California, December 1989.
- Liebelt, P. B., *An Introduction To Optimal Estimation*, Addison Wesley, Inc., 1967.
- Lynch, J. F., R. C. Spindel, C. S. Chiu, J. H. Miller, and T. G. Birdsall, "Results from the 1984 Marginal Ice Zone Experiment Preliminary Tomography Transmissions:

Implications for Marginal Ice Zone, Arctic, and Surface Wave Tomography". *Journal of Geophysical Research*, 92(C7), 6869-6885, 1987.

Mackenzie, K. V., "Nine-term Equation for Sound Speed in the Ocean", *Journal of the Acoustical Society of America*, 70, 807, 1981.

Meinke, J., "The Greenland Sea Project - A Venture towards Better Understanding of the Role of the Greenland Sea in Ocean Climate", International Council for Exploration of the Sea, 1989.

Munk, W. and C. Wunsch, "Ocean Acoustic Tomography: A Scheme for Large Scale Monitoring", *Deep Sea Research, Part A*, 26, 123-161, 1979.

Pawlowicz, R., Woods Hole Oceanographic Institute, Personal Communication to C. S. Chiu, Subject: Greenland Sea Project Data, 22 Mar 1991.

Spindel, R. C., "Signal Processing in Ocean Tomography", *Adaptive Methods in Underwater Acoustics*, D. Reidel, 1985.

Ugincius, P. "Ray Acoustic and Fermat's Principle in a Moving Inhomogeneous Medium", *The Journal of the Acoustic Society of America*, 51, 1759-1763, 1970.

Wiggins, R. A., "The General Linear Inverse Problem: Implications of Surface Waves and Free Oscillations for Earth Structure", *Reviews of Geophysics and Space Physics*, 10, 251-285, 1972.

Worcester, P. E. and B. M. Howe, *GSP88/MST88: Deployment Cruise Summary*, 01 Feb 1989.

Ziomek, L. J., *Underwater Acoustics A Linear Systems Theory Approach*, Academic Press, Inc., 1985.

INITIAL DISTRIBUTION LIST

	No. Copies
1. Defense Technical Information Center Cameron Station Alexandria, VA 22304-6145	2
2. Library, Code 52 Naval Postgraduate School Monterey, CA 93943-5002	2
3. Chairman (Code OC, Co) Department of Oceanography Naval Postgraduate School Monterey, CA 93943-5000	1
4. Library Scripps Institution of Oceanography P. O. Box 2367 La Jolla, CA 92037	1
5. Professor Ching-Sang Chiu (Code OC/Ci) Department of Oceanography Naval Postgraduate School Monterey, CA 93943-5000	2
6. Professor Jeffrey A. Nystuen (Code OC/Ny) Department of Oceanography Naval Postgraduate School Monterey, CA 93943-5000	1
7. Professor James F. Lynch Department of Applied Ocean Physics and Engineering Woods Hole Oceanographic Institute Woods Hole, MA 02543	1
8. Director Naval Oceanography Division Naval Observatory 34th and Massachusetts Avenue NW Washington, DC 20390	1
9. Commander Naval Oceanography Command Stennis Space Center MS 39529-5000	1
10. Commanding Officer Naval Oceanographic and Atmospheric	1

Research Laboratory
Stennis Space Center
MS 39529-5004

- | | | |
|-----|--|---|
| 11. | Office of Naval Research (Code 420)
Naval Ocean Research and Development
Activity
800 N. Quincy Street
Arlington, VA 22217 | 1 |
| 12. | LT John E. Joseph
USS Peleliu (LHA-5)
FPO San Francisco, CA 96624-1620 | 1 |

Thesis

J8264 Joseph

c.1 Acoustic tomography in
the Greenland Sea.

Thesis

J8264 Joseph

c.1 Acoustic tomography in
the Greenland Sea.

DUDLEY KNOX LIBRARY



3 2768 00014764 9